

# Topology- and error-driven extension of scalar functions from surfaces to volumes

Giuseppe Patanè  
CNR-IMATI \*

Michela Spagnuolo  
CNR-IMATI

Bianca Falcidieno  
CNR-IMATI

## Abstract

The behavior of a variety of phenomena measurable on the boundary of 3D shapes is studied by modelling the set of known measurements as a scalar function  $f : \mathcal{P} \rightarrow \mathbb{R}$ , defined on a surface  $\mathcal{P}$ . Furthermore, the large amount of scientific data calls for efficient techniques to correlate, describe, and analyze this data. In this context, we focus on the problem of extending the measures captured by a scalar function  $f$ , defined on the boundary surface  $\mathcal{P}$  of a 3D shape, to its surrounding volume. This goal is achieved by computing a sequence of volumetric functions that approximate  $f$  up to a specified accuracy and preserve its critical points. More precisely, we compute a smooth map  $g : \mathbb{R}^3 \rightarrow \mathbb{R}$  such that the piecewise linear function  $h := g_{\mathcal{P}} : \mathcal{P} \rightarrow \mathbb{R}$ , which interpolates the values of  $g$  at the vertices of the triangulated surface  $\mathcal{P}$ , is an approximation of  $f$  with the same critical points. In this way, we overcome the limitation of traditional approaches to function approximation, which are mainly based on a numerical error estimation and do not provide measurements of the topological and geometric features of  $f$ . The proposed approximation scheme builds on the properties of  $f$  related to its *global structure*, i.e. its critical points, and ignores the local details of  $f$ , which can be successively introduced according to the target approximation accuracy.

**CR Categories:** I.3.5 [Computational Geometry and Object Modeling]: Boundary representations—Curve, surface, solid, and object representations; G.1.2 [Approximation]: Approximation of surfaces and contours.

**Keywords:** Critical points, topological and geometric algorithms, surface/volume-based decompositions and visualization, 2D scalar functions, topological simplification, computational topology.

## 1 Introduction

Given a scalar function  $f : \mathcal{P} \rightarrow \mathbb{R}$ , defined on a surface  $\mathcal{P}$ , we address the problem of defining a map  $g : \mathcal{P} \rightarrow \mathbb{R}$ , which extends  $f$  from  $\mathcal{P}$  to  $\mathbb{R}^3$  by computing a sequence of volumetric functions that approximate  $f$  up to a specified accuracy and preserve its critical points. The implicit map  $g$  is the superposition of a set of basis functions, generated by a kernel  $\varphi \in C^k$ , so that the order of smoothness of  $g$  is  $k$ . The novelty of our approach resides in the use of the critical points of  $f$  to drive the approximation process: this choice allows us to use a relatively small amount of basis functions and provides an easy control on the local details and the degree of smoothness of the final approximation.

The large amount of scientific data available nowadays in digital form calls for efficient techniques to correlate, describe, and analyze this data. Most frequently, scientific data correspond to measurements or sampling of scalar functions that model the behavior of a variety of phenomena measurable on the boundary of a 3D shape. For example, in geographical data analysis a terrain

model is associated to an elevation map; in engineering, scalar functions are generated by solving differential equations related to simulation problems (e.g., the Laplace and heat equation [Belkin and Niyogi 2003; Ni et al. 2004]) or decomposing the spectrum of data-dependent kernels [Belkin and Niyogi 2003].

A volume-based approximation of  $f : \mathcal{P} \rightarrow \mathbb{R}$ , which gives an insight into the behaviour of  $f$  in the space where  $\mathcal{P}$  is embedded, could be useful to make predictions about the phenomenon or analyze their reactivity to other entities. For instance, the approximation of spatio-physico-chemical properties measured or simulated on a molecular surface  $\mathcal{P}$  to the surrounding volume could be used to predict the interactions among proteins [Cipriano and Gleicher 2007]. Other examples of  $f$  are the electrostatic charge, hydrophobicity, temperature, and pressure. Also, a volume-based approximation of  $f$  enables to couple the analysis of the behaviour of its iso-contours with the corresponding iso-surfaces of the volumetric approximation.

Recent research work addresses the problem of converting surface data to volumetric one: volumetric functions have been used to parameterize 3D shapes for trivariate B-spline fitting [Martin et al. 2008] and solid modeling applications such as tetrahedral remeshing and solid texture mapping [Li et al. 2007]. For instance, in [Martin et al. 2008] the iso-parametric paths [Dong et al. 2006] of two orthogonal harmonic functions on a 0-genus surface  $\mathcal{P}$  provide a parameterization grid that is used to fit  $\mathcal{P}$  with a trivariate B-spline. Our approach builds on implicit modeling techniques, can be applied to surfaces with arbitrary genus, is more flexible with respect to the smoothness properties of  $f$ , and does not require a parameterization domain.

Traditional approaches to function approximation are mainly driven by a numerical error estimation: from our perspective, instead, the critical points are a natural choice to guide the approximation scheme as they usually represent very relevant information about the phenomena coded by  $f$ . For instance, in biomolecular simulation the maxima of the electrostatic charge are those features that guide the interaction and that should be preserved for a correct analysis of the phenomenon. Approximating the electrostatic charge on a molecular surface without preserving the distribution of its maxima and minima introduces artifacts in the modeling of those interactions that are guided by the energy extrema. By preserving the shape of the input scalar function through its critical points, it is also possible to devise an approximation scheme that allows us to distinguish the *global structure* of  $f$  from local details, which can be preserved or discarded according to the target accuracy.

More precisely, given a 2-manifold triangle mesh  $\mathcal{P}$  in  $\mathbb{R}^3$  and a set of scalar values at the vertices  $M := \{\mathbf{p}_i\}_{i=1}^n$  of  $\mathcal{P}$ , let us consider the piecewise linear map  $f : \mathcal{P} \rightarrow \mathbb{R}$  that interpolates these values over  $\mathcal{P}$ . Our aim is to compute a smooth function  $g : \mathbb{R}^3 \rightarrow \mathbb{R}$  such that the piecewise linear map  $g_{\mathcal{P}}$ , which interpolates the values of  $g$  at the vertices of  $\mathcal{P}$ , approximates  $f$  within a prescribed error and preserves its critical points. The approximation scheme computes  $g := g_1 + g_2$  as the sum of two components  $g_1, g_2 : \mathbb{R}^3 \rightarrow \mathbb{R}$  such that

1.  $g_1$  captures the global structure of  $f$  in terms of its critical points, that is, the piecewise linear scalar function  $f_1 := g_{1,\mathcal{P}}$

---

\*Istituto di Matematica Applicata e Tecnologie Informatiche, Consiglio Nazionale delle Ricerche, Genova, Italy. E-mail: {patane, spagnuolo, falcidieno}@ge.imati.cnr.it

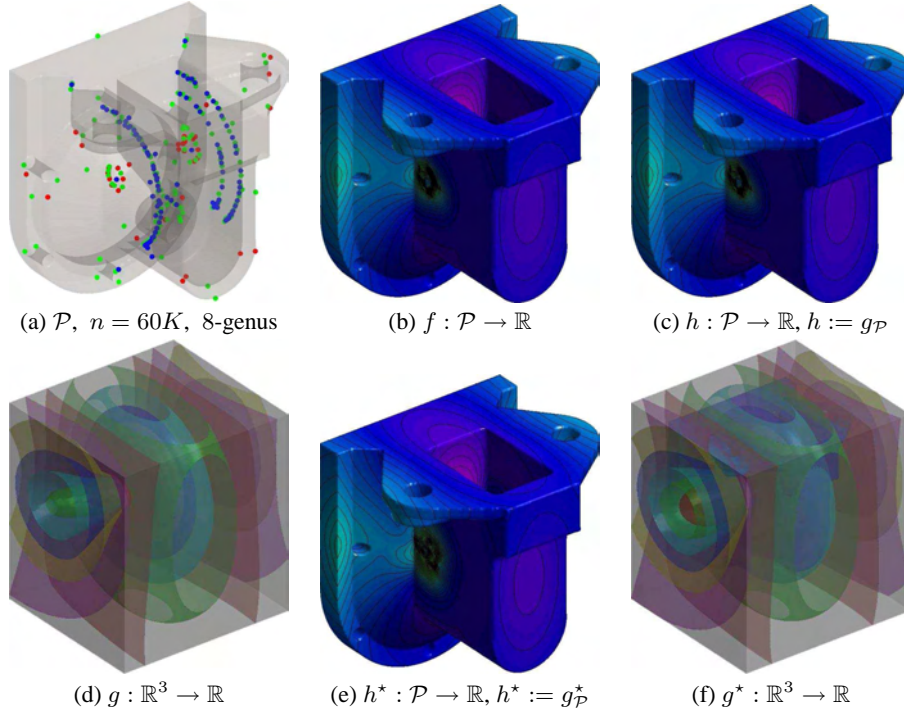


**Figure 1:** Overview of the proposed approach. (a) Critical points ( $M = 99$ ,  $m = 35$ ,  $s = 148$ ) and (b) level sets of a stress function  $f$  on a mechanical surface  $\mathcal{P}$ . Here,  $M$ ,  $m$ , and  $s$  is the number of maxima, minima, and saddles. (c) Level sets of its approximation  $h := g_{\mathcal{P}}$  achieved by using  $r = 1924$  globally-supported basis functions:  $f$  and  $h$  have the same critical points and the  $L^\infty$ -error between  $f$  and  $h$  is 0.094. (d) Iso-surfaces of the volume-based approximation  $g : \mathbb{R}^3 \rightarrow \mathbb{R}$  of  $f$ . (e) Level sets of the function  $h^*$  computed using a simplified set of critical points (i.e.,  $M = 28$ ,  $m = 8$ , and  $s = 50$  critical points) and  $r = 1011$  globally-supported radial basis functions. (f) Iso-surfaces of the volume-based approximation  $g^*$  of  $h^*$ ; comparing (b) with (e) and (d) with (f) we see that the level sets share a common behavior around  $\mathcal{P}$ . (h) Distribution of the  $L^\infty$ -error between  $f$  and  $h^*$ , where  $\|f - h^*\|_\infty = 0.017$  (red areas).

that interpolates the values of  $g_1$  at the vertices of  $\mathcal{P}$  has the same critical points of  $f$ . On the basis of this property, we refer to  $f_1$  as the *global component* of  $f$ ;

2.  $g_2$  recovers the local details of  $f$ ; i.e., the piecewise linear scalar function  $f_2 := g_{2,\mathcal{P}}$ , which interpolates the values of  $g_2$  at the vertices of  $\mathcal{P}$ , guarantees that the error between  $f$  and  $f_1 + f_2$  is below the target approximation accuracy. On the basis of this property, we refer to  $f_2$  as the *local component* of  $f$ .

The function  $g_1$  is computed as a linear combination of globally-supported radial basis functions [Aronszajn 1950; Bloomenthal and Wyvill 1997; Dyn et al. 1986; Poggio and Girosi 1990], whose centers are selected through an iterative procedure which converges in a generally low number of steps. The function  $g_2$  is generated as a linear combination of locally-supported radial basis functions, using as error metric the  $L^\infty$ -norm or a local comparison measure [Biasotti et al. 2007; Edelsbrunner et al. 2004].

An important constraint on  $g$  is its global support. In fact, using only compactly-supported basis functions would provide a map  $g$  with several and small iso-surfaces that have artifacts where the supports of the basis functions intersect. Therefore, the use of a compact support results in a poor visualization of  $g$  and a coarse approximation of  $f$  on  $\mathcal{P}$ . Furthermore, the support selection is not trivial and a local definition of  $g$  would not extrapolate the behavior of  $f$  on the interior and exterior of  $\mathcal{P}$ . On the contrary, using globally supported radial basis functions cannot result in wrong blends and the kernel variance can be adapted to the local sampling density and geometry [Dey and Sun 2005; Mitra and Nguyen 2003].

The proposed approximation scheme handles scalar functions defined on surfaces represented by 2-manifold triangle meshes without imposing constraints on the sampling density. The choice of globally- and compactly-supported radial basis functions enable to adapt the construction of the approximation to specific problem constraints, such as the number of input samples, the local accuracy, and the degree of smoothness of the final approximation. The approximation method can also be used to smooth the function  $f$  by selecting only the critical points which are perceived as informative ones. For instance,  $f$  might exhibit *differential noise*, that is, a high number of critical points with very close positions and low variation of the  $f$ -values, due to a low quality of the discrete representations of the input data, unstable computations, or noisy measurements.

The approximation can be run only on a subset of critical points; for instance, those considered relevant by persistence-based simplification methods [Edelsbrunner et al. 2004], Laplacian [Patanè and Falcidieno 2009; Taubin 1995] and Gaussian smoothing operators [Liu et al. 2007]. We will show how the relevant critical points of  $f$  contain enough information to define a *topology-driven* approximation of  $f$  in a computationally efficient way. If necessary, the approximation  $f_1$  of  $f$  can be improved by adding to  $g_1$  the local component, that is, the *error-driven* term  $g_2$  so that the error between  $f_1 + g_{2,\mathcal{P}}$  and  $f$  is below the target approximation accuracy. To show the flexibility of the proposed approach, we also derive a least-squares and a constrained approximation scheme. Figure 1 and 2 show the main steps of the entire framework.

This article is organized as follows: Section 2 briefly reviews previous work on the analysis of scalar functions and implicit approx-

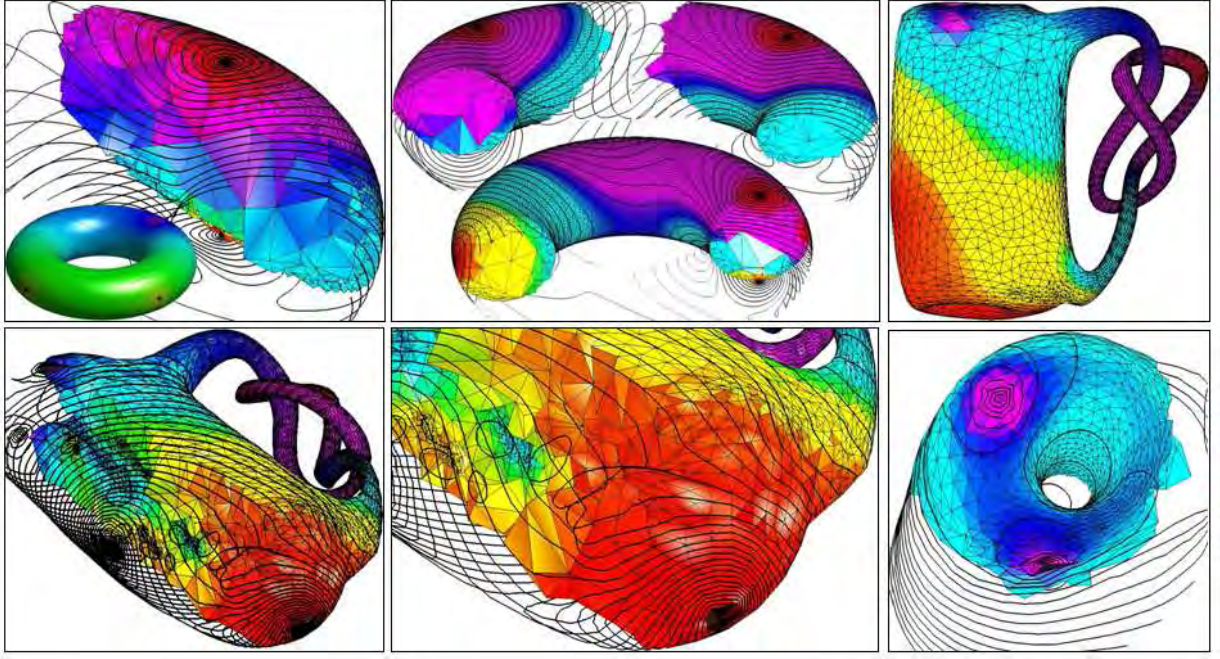


**Figure 2:** Level sets of a map  $f : \mathcal{P} \rightarrow \mathbb{R}$  and its volumetric approximation  $g : \mathbb{R}^3 \rightarrow \mathbb{R}$ . The map  $g$  is a superposition of functions centered at a set of points on  $\mathcal{P}$  and has been sampled on a tetrahedralization of  $\mathcal{P}$ . Both  $f$  and  $g_{\mathcal{P}}$  have the same critical points.

imation. In Section 3, we discuss how to build smooth approximations of  $f$  on  $\mathcal{P}$ . In Section 4, we focus the analysis of  $f$  on specific properties, related to its global structure, and neglect local details, which are successively introduced according to the target approximation accuracy. In Section 5, we analyse the main properties of the surface- and volume-based approximating functions. In Section 6, we discuss the application of the method to the simplification and visualization of scalar functions, and also detail the degrees of freedom of the proposed approach. Finally, future work is discussed in Section 7.

## 2 Theoretical background and previous work

This section introduces the theoretical background on the representation and analysis of scalar functions defined on triangulated surfaces (Section 2.1); then, we briefly review previous work on implicit approximation (Section 2.2).

### 2.1 Theoretical background

The key concepts used in the presentation of the proposed approach are those related to the triangle-based representation of scalar function, to the classification of critical points, and to the evaluation of the approximation error. We summarize here the basic definitions and refer the reader to [Biasotti et al. ; Bloomenthal and Wyvill 1997] for a complete discussion.

A map  $\tilde{f} : \mathcal{M} \rightarrow \mathbb{R}$  of class  $\mathcal{C}^2$ , defined on a smooth manifold  $\mathcal{M}$ , is *Morse* if it has no degenerate critical points (i.e., the Hessian matrix is not singular at the critical points of  $f$ ). In the following, we replace  $\tilde{f}$  with a piecewise linear scalar function  $f : \mathcal{P} \rightarrow \mathbb{R}$  over a triangulation  $\mathcal{P} := (M, T)$  of  $\mathcal{N}$ , where  $M := \{\mathbf{p}_i\}_{i=1}^n$  is a set of  $n$  vertices and  $T$  is an *abstract simplicial complex* that contains the adjacency information. The function  $f$  on  $\mathcal{P}$  is defined by linearly interpolating

the values  $(f(\mathbf{p}_i))_{i=1}^n$  of  $f$  at the vertices using barycentric coordinates. Assuming that  $t := (\mathbf{p}_i, \mathbf{p}_j, \mathbf{p}_k)$  is a triangle of  $\mathcal{P}$  with vertices  $\mathbf{p}_i, \mathbf{p}_j, \mathbf{p}_k$ , the value  $f(\mathbf{p})$ ,  $\mathbf{p} \in t$ , is defined as  $f(\mathbf{p}) := \lambda_1 f(\mathbf{p}_i) + \lambda_2 f(\mathbf{p}_j) + \lambda_3 f(\mathbf{p}_k)$ , where  $\lambda_1, \lambda_2, \lambda_3 \geq 0$ ,  $\lambda_1 + \lambda_2 + \lambda_3 = 1$ , are the barycentric coordinates of  $\mathbf{p}$  with respect to the vertices of  $t$ . If  $f(\mathbf{p}_i) \neq f(\mathbf{p}_j)$ , for each edge  $(i, j)$ , then  $f$  is called *general*. Finally, we assume that  $f$  is general and degenerate cases will be discussed in Section 6.3.

As  $\alpha \in \mathbb{R}$  varies, the behavior of  $f$  is conveyed by the corresponding level sets  $\gamma_\alpha$  and the critical points of  $f$ , at which the number of connected components of the level sets changes. The critical points of  $f : \mathcal{P} \rightarrow \mathbb{R}$  are computed by analyzing the distribution of the  $f$ -values on the neighborhood of each vertex  $\mathbf{p}_i$  [Banchoff 1967]. More precisely, let  $N(i) := \{j : (i, j) \text{ edge}\}$  be the 1-star of  $i$ , i.e. the set of vertices incident to  $i$ . Formally, if we let

$$Lk(i) := \{j_1, \dots, j_k \in N(i) : (j_s, j_{s+1})_{s=1}^{k-1} \text{ edges of } \mathcal{P}\}$$

be the *link* of  $i$  then the *upper link* is the set

$$Lk^+(i) := \{j_s \in Lk(i) : f(\mathbf{p}_{j_s}) > f(\mathbf{p}_i)\},$$

and the *mixed link* is given by

$$Lk^\pm(i) := \{j_s \in Lk(i) : f(\mathbf{p}_{j_{s+1}}) > f(\mathbf{p}_i) > f(\mathbf{p}_{j_s}) \text{ or } f(\mathbf{p}_{j_{s+1}}) < f(\mathbf{p}_i) < f(\mathbf{p}_{j_s})\},$$

where  $j_{k+1} := j_k$ . The *lower link*  $Lk^-(i)$  is defined by replacing the inequality “>” with “<” in the upper link. If  $Lk^+(i) = \emptyset$  or  $Lk^-(i) = \emptyset$ , then  $\mathbf{p}_i$  is a *maximum* or a *minimum*, respectively. If the cardinality of the set  $Lk^\pm(i)$  is  $2 + 2m$ ,  $m \geq 1$ , then  $\mathbf{p}_i$  is classified as a *saddle of multiplicity*  $m$ .

For a closed surface  $\mathcal{P}$  and a general function  $f$ , the identity

$$\chi(\mathcal{P}) = m - s + M, \quad (1)$$

gives the relation between the critical points of  $(\mathcal{P}, f)$  and the Euler characteristic  $\chi(\mathcal{P})$  of  $\mathcal{P}$  [Banchoff 1967; Milnor 1963]. Note that  $s$  is the number of saddles counted with their multiplicity, i.e.  $s := \sum_{\mathbf{p}_i \text{ saddle}} m_i$ , where  $m_i$  is the multiplicity of the saddle  $\mathbf{p}_i$ .

**Comparison of scalar functions.** Since the level sets and critical points are independent of positive re-scalings of  $f$ , we assume that the function values have been normalized in such a way that  $\text{Image}(f) = [0, 1]$ . The  $L^\infty$ -approximation error between two functions  $f_1, f_2 : \mathcal{P} \rightarrow \mathbb{R}$  is defined as  $\|f_1 - f_2\|_\infty := \max_{i=1, \dots, n} \{|f_1(\mathbf{p}_i) - f_2(\mathbf{p}_i)|\}$ . In the article pictures, the  $L^\infty$ -error is coded with colors that range from red (maximum error) to blue (null error).

A number of local and global comparison measures [Biasotti et al. 2007; Edelsbrunner et al. 2004], based on the differential and geometric properties of the level sets, are alternative to the  $L^\infty$ -norm. More precisely, the comparison measure between two scalar functions  $f_1, f_2 : \mathcal{P} \rightarrow \mathbb{R}$ , on the same surface  $\mathcal{P}$ , is defined as the averaged angle variation of their gradient fields [Biasotti et al. 2007], i.e.  $\mathcal{I}(f_1, f_2) : \mathcal{P} \rightarrow \mathbb{R}$ ,  $\mathcal{I}(f_1, f_2) := \langle \nabla f_1, \nabla f_2 \rangle$ . As an alternative, in [Edelsbrunner et al. 2004] the comparison measure  $\mathcal{I}(f_1, f_2) := \|\nabla f_1 \wedge \nabla f_2\|_2$  is the norm of the wedge product of the gradient fields. The main difference between [Biasotti et al. 2007] and [Edelsbrunner et al. 2004] is that the former provides an explicit relation between the critical points of  $f_1, f_2$ , and  $\mathcal{I}(f_1, f_2)$ . In both cases, the averaged error measure between  $f_1$  and  $f_2$  on  $\mathcal{P}$  is  $\bar{\mathcal{I}}(f_1, f_2) := \frac{1}{\text{area}(\mathcal{P})} \int_{\mathcal{P}} \mathcal{I}(f_1, f_2) d\mathbf{p}$ .

## 2.2 Previous work

In implicit modeling [Bloomenthal and Wyvill 1997], a 3D point set  $\mathcal{L} := \{\mathbf{p}_i \in \mathbb{R}^3 : i = 1, \dots, n\}$  is approximated by the surface  $\Sigma := \{\mathbf{p} \in \mathbb{R}^3 : g(\mathbf{p}) = 0\}$ , where  $g : \mathbb{R}^3 \rightarrow \mathbb{R}$  is an implicit function. In this context, implicit approximation techniques [Aronszajn 1950; Dyn et al. 1986; Micchelli 1986; Poggio and Girosi 1990] compute  $g(\mathbf{p}) := \sum_{i=1}^n \alpha_i \varphi_i(\mathbf{p})$  as a linear combination of the basis elements  $\mathcal{B} := \{\varphi(\|\mathbf{p} - \mathbf{p}_i\|_2)\}_{i=1}^n$ , where  $\varphi$  is the kernel function. Depending on the properties of  $\varphi$  and of the corresponding approximation scheme, we distinguish globally- [Carr et al. 2001; Turk and O'Brien 2002] and compactly- [Wendland 1995; Morse et al. 2001; Ohtake et al. 2005a] supported radial basis functions, and the partition of unity [Ohtake et al. 2003; Xie et al. 2004]. We briefly remind that the *support* of an arbitrary map  $g : \mathbb{R}^3 \rightarrow \mathbb{R}$  is defined as the set  $\text{supp}(g) := \{\mathbf{p} \in \mathbb{R}^3 : g(\mathbf{p}) \neq 0\}$ . If  $\text{supp}(g) := \mathbb{R}^3$ , then  $g$  has *global support*.

To reduce the amount of memory storage and computation time of the implicit approximation, sparsification methods select a subset of centers in  $\mathcal{L}$  such that the associated function  $g$  approximates  $\mathcal{L}$  within a target accuracy. This aim is usually achieved through *a-posteriori* updates of the approximating function, which are guided by the local approximation error [Carr et al. 2001; Chen and Wigger 1995; Kanai et al. 2006; Ohtake et al. 2005b; Shen et al. 2004], or by solving a constrained optimization problem [Girosi 1998; Patanè 2006; Steinke et al. 2005; Walder et al. 2006].

Clustering techniques can also be used to group those points that satisfy a common “property” and center a basis function at a representative point of each cluster. Main clustering criteria are the planarity and closeness, measured in the Euclidean space using the  $k$ -means clustering [Lloyd 1982] and the principal component analysis [Jolliffe 1986] (PCA, for short). As an alternative, kernel methods [Cortes and Vapnik 1995] evaluate the correlation among points with respect to the scalar product induced by a positive-definite kernel. In this case, the PCA and the  $k$ -means algorithm

lead to efficient clustering techniques such as the kernel PCA and the Voronoi tessellation of the feature space [Schoelkopf and Smola 2002] (Ch. 1).

Recently, Gaussian radially symmetric [Co et al. 2003; Jang et al. 2004; Weiler et al. 2005] and ellipsoidal [Jang et al. 2006; Hong et al. 2006] basis functions have been used to approximate 3D scalar maps. The variance and width parameters of ellipsoidal basis functions, which are best suited to fit data that is not radially symmetric, are computed using the Levenberg-Marquardt optimization method [Madsen et al. 2004]. In both cases, the centers of the basis functions are selected by clustering techniques or an error-driven scheme, which add the points with the maximum error values as new centers. The iteration stops when the approximation error is below a given threshold. As discussed in [Weiler et al. 2005], the set of centers can be enriched by including the peaks and low frequency regions of the input data.

## 3 Topology-driven approximation

This section discusses the core of our approach and is organized as follows. In Section 3.1 and 3.2, we describe how a scalar function  $f : \mathcal{P} \rightarrow \mathbb{R}$  is approximated by a map  $h := g_{1,\mathcal{P}}$  such that  $f$  and  $h$  have the same critical points. We refer to  $h$  as the *global component* of  $f$ . The piecewise linear function  $h$  interpolates the values of the implicit map  $g_1 : \mathbb{R}^3 \rightarrow \mathbb{R}$  at the vertices of  $\mathcal{P}$  and  $g_1$  is computed as a linear combination of globally-supported radial basis functions. The centers of the basis functions are selected through an iterative procedure, which is guided by the information conveyed by the critical points of  $f$  and converges in a low number of steps.

In Section 4, the approximation  $h$  of  $f$  is improved by adding an error-driven term  $g_2$  to  $g_1$  such that the error between  $h + g_{2,\mathcal{P}}$  and  $f$  is below the target approximation accuracy. In this case,  $g_2$  is a linear combination of locally-supported functions and the center selection is guided by the target approximation accuracy.

### 3.1 Proposed approach

We formulate the approximation of a piecewise linear scalar function  $f : \mathcal{P} \rightarrow \mathbb{R}$ , defined on the 2-manifold triangle mesh  $\mathcal{P}$ , in such a way that we preserve its critical points. To this end, we focus our attention on the following problem.

**Problem statement.** Find a smooth function  $g_1 : \mathbb{R}^3 \rightarrow \mathbb{R}$  with global support such that the piecewise linear function  $h := g_{1,\mathcal{P}} : \mathcal{P} \rightarrow \mathbb{R}$ , which interpolates the values of  $g_1$  at the vertices of  $\mathcal{P}$  (i.e.,  $h(\mathbf{p}_i) := g_1(\mathbf{p}_i)$ ,  $i = 1, \dots, n$ ), satisfies the following conditions:

1.  $f$  and  $h$  have exactly the same critical points;
2.  $h$  has fair level sets with a regular distribution on  $\mathcal{P}$ .

Let  $\{\mathbf{p}_i, i \in \mathcal{C}\}$  be the set of critical points of  $f$ . At the level  $k = 1$  (Figure 3(a,b)), we search a function  $g^{(1)} : \mathbb{R}^3 \rightarrow \mathbb{R}$  such that

$$g^{(1)}(\mathbf{p}_j) := f(\mathbf{p}_j), \quad i \in \mathcal{I}^{(1)} := \mathcal{C} \cup \{j \in N(i), i \in \mathcal{C}\}, \quad (2)$$

i.e., we impose that  $f$  and  $g^{(1)}$  have the same values at the critical points of  $f$  and at the vertices of the corresponding 1-stars. In the following, we assume that the indices are without repetitions.

We compute  $g^{(1)}$  using an implicit interpolation scheme. Choosing a kernel  $\varphi : \mathbb{R}^+ \rightarrow \mathbb{R}$ ,  $g^{(1)}$  is defined as [Aronszajn 1950; Poggio and Girosi 1990]

$$g^{(1)}(\mathbf{p}) := \sum_{i \in \mathcal{I}^{(1)}} \alpha_i \varphi_i(\mathbf{p}) + \pi(\mathbf{p}), \quad \mathbf{p} := (x, y, z), \quad (3)$$



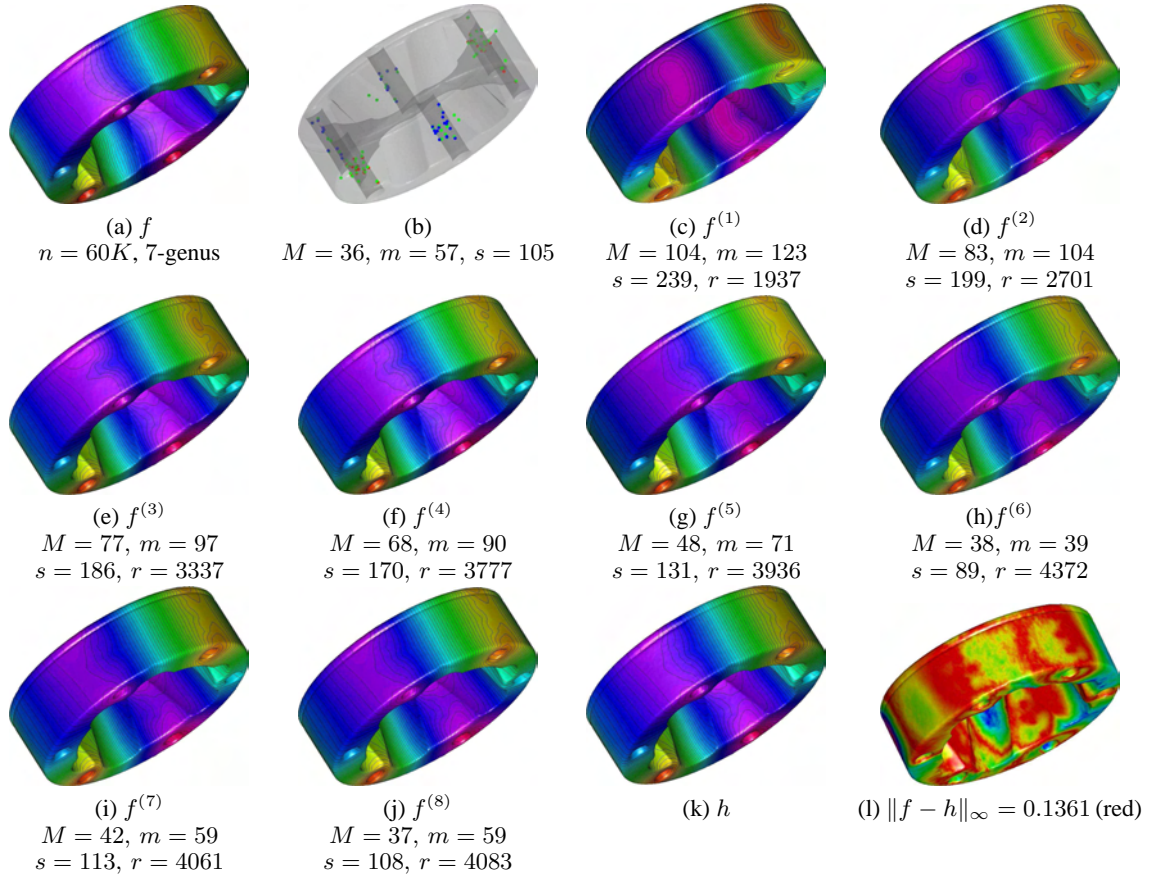


**Figure 3:** (a) Color map, level sets, and (b) critical points of a stress function  $f$  on a mechanical surface  $\mathcal{P}$ . (c-j) Level sets, number of critical points, and selected centers of the approximation  $f^{(k)}$  of  $f$ ,  $k = 1, \dots, 8$ . From the first (c) to the fourth (f) iteration, the current approximation of  $f$  shows evident changes with respect to the previous one; from the fifth (g) to the eighth (j) iteration, the shape of the level sets slightly varies. (k) Final approximation  $h$  of  $f$ :  $f$  and  $h$  have the same critical points. Comparing (a) with (k), we see that  $h$  accurately and smoothly resembles the global behavior of  $f$ ; the distribution of the  $L^\infty$ -error between  $f$  and  $h$  is shown in (l). See also Figure 4.

that is, a linear combination of the radial basis functions  $\varphi_i(\mathbf{p}) := \varphi(\|\mathbf{p} - \mathbf{p}_i\|_2)$ , centered at  $\{\mathbf{p}_i, i \in \mathcal{I}^{(1)}\}$ , plus a first-degree polynomial  $\pi(\mathbf{p}) := \beta_0 + \beta_1 x + \beta_2 y + \beta_3 z$ . Common choices of  $\varphi$  are the Gaussian  $\varphi(t) := \exp(-t)$  and the bi-harmonic  $\varphi(t) := |t|^3$  kernel.

The second term  $\pi$  in (3) is used to fit  $f$  over regions of  $\mathcal{P}$  where it is linear. Without loss of generality, we set  $\mathcal{I}^{(1)} = \{1, \dots, r_1\}$ ; then, the coefficients in (3) that uniquely satisfy (2) are the solution of the following  $(r_1 + 4) \times (r_1 + 4)$  square linear system

$$\underbrace{\begin{bmatrix} a_{11} & \dots & a_{1r_1} & p_1^x & p_1^y & p_1^z & 1 \\ \vdots & \ddots & \vdots & \vdots & \vdots & \vdots & \vdots \\ a_{r_1 1} & \dots & a_{r_1 r_1} & p_{r_1}^x & p_{r_1}^y & p_{r_1}^z & 1 \\ p_1^x & \dots & p_{r_1}^x & 0 & 0 & 0 & 0 \\ p_1^y & \dots & p_{r_1}^y & 0 & 0 & 0 & 0 \\ p_1^z & \dots & p_{r_1}^z & 0 & 0 & 0 & 0 \\ 1 & \dots & 1 & 0 & 0 & 0 & 0 \end{bmatrix}}_{\tilde{\mathbf{L}}^{(1)}} \sigma_1 = \begin{bmatrix} f(\mathbf{p}_1) \\ \vdots \\ f(\mathbf{p}_{r_1}) \\ 0 \\ 0 \\ 0 \\ 0 \end{bmatrix} \quad (4)$$

$$\sigma_1 := [\alpha_1 \quad \dots \quad \alpha_{r_1} \quad \beta_0 \quad \beta_1 \quad \beta_2 \quad \beta_3]^T,$$

with  $a_{ij} := \varphi(\|\mathbf{p}_i - \mathbf{p}_j\|_2)$  and  $\mathbf{p}_i := (p_i^x, p_i^y, p_i^z)$ . The last four rows of the full matrix in (4) correspond to the *natural additional*

*constraints*

$$\sum_{i=1}^{r_1} \alpha_i p_i^x = 0, \quad \sum_{i=1}^{r_1} \alpha_i p_i^y = 0, \quad \sum_{i=1}^{r_1} \alpha_i p_i^z = 0.$$

These relations guarantee that  $\tilde{\mathbf{L}}^{(1)}$  is invertible; in fact, the  $r_1 \times r_1$  sub-matrix  $\mathbf{A} := (a_{ij})_{i,j}$  is conditionally positive-definite on the subspace of vectors that are orthogonal to the last four rows of the full matrix. Once we have calculated  $g^{(1)}$ , the piecewise linear scalar function  $f^{(1)} := g_{\mathcal{P}}^{(1)} : \mathcal{P} \rightarrow \mathbb{R}$  is a new map that approximates  $f$  (Figure 3(c)).

We explicitly note that the constraints in (2) guarantee that each critical point of  $f$  is also critical for  $f^{(1)}$ ; if  $f^{(1)}$  has additional critical points, then they will be used to build the new approximation of  $f$ . If  $\mathcal{C}^{(1)}$  are the indices of the critical points of  $f^{(1)}$ , then  $\mathcal{Q}^{(1)} := \{\mathbf{p}_i, i \in \mathcal{C}^{(1)}, i \notin \mathcal{I}^{(1)}\}$  can be interpreted as the set of points where the current approximation  $f^{(1)}$  differs from  $f$  with respect to the point of view of the critical points distribution.

At the next step  $k = 2$ , the points in  $\mathcal{Q}^{(1)}$  are used to improve the current approximation  $f^{(1)}$  of  $f$ . More precisely, we calculate the function  $g^{(2)}$  that satisfies the previous interpolating conditions (2)

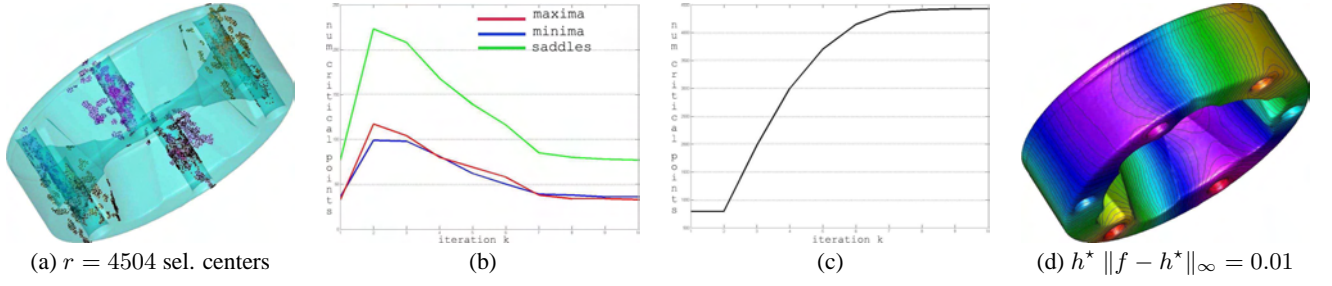


**Figure 4:** (a) Centers used to compute the approximation in Figure 3(k) (i.e., the 0.06% of the input vertices). Variation of (b) the number of critical points and (c) selected centers of  $f^{(k)}$  at each iteration. (d) Level sets of  $h^*$  achieved by summing to the approximation  $h$  in Figure 3(k) 1928 locally-supported basis functions.

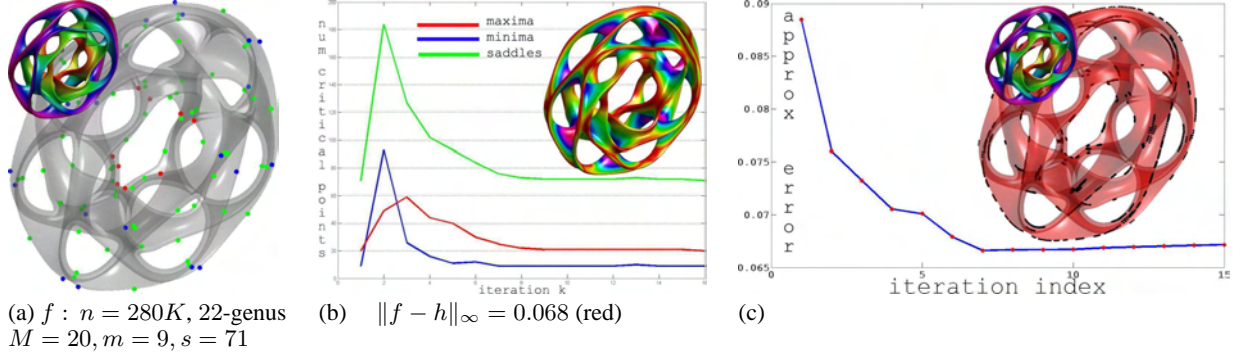


**Figure 5:** (a) Color map, level sets, and number of critical points of a scalar function  $f$  on a 22-genus surface  $\mathcal{P}$ . (b) Variation of the number of critical points and distribution of the  $L^\infty$ -error between  $f$  and  $h$  on  $\mathcal{P}$  (top). Statistic values are reported in Table 1. (c) Plot of the error  $\|f - f^{(k)}\|_\infty, k = 1, \dots, 15$ . The final approximation  $h$  of  $f$  has been computed with 2789 centers (i.e., the 0.01% of the input vertices). The level sets of  $h$  and selected centers are shown in the top part of (c).

---

**Algorithm 1** Main steps of the topology-driven approximation.

---

**Require:** A scalar function  $f : \mathcal{P} \rightarrow \mathbb{R}$  defined on the triangulated surface  $\mathcal{P}$ .

**Ensure:** The implicit function  $g : \mathbb{R}^3 \rightarrow \mathbb{R}$  such that  $h := g_{\mathcal{P}}$  has the same critical points  $\mathcal{C}$  of  $f$ .

- 1: Extract and store the 1-star of each vertex of  $\mathcal{P}$ .
  - 2: Set  $k := 0, \mathcal{C}^{(0)} := \emptyset, \mathcal{I}^{(0)} = \emptyset, f^{(0)} := f$ .
  - 3: **while**  $\mathcal{C}^{(k)} \neq \mathcal{C}$  **do**
  - 4:   compute the set  $\mathcal{C}^{(k)}$  of critical points of  $f^{(k)}$ ;
  - 5:    $\mathcal{Q}^{(k)} := \{i \in \mathcal{C}^{(k)}, i \notin \mathcal{I}^{(k)}\}$ ;
  - 6:    $\mathcal{T}^{(k)} := \{j \in N(i), i \in \mathcal{Q}^{(k)}\}$ ;
  - 7:    $\mathcal{I}^{(k+1)} := \mathcal{I}^{(k)} \cup \mathcal{Q}^{(k)} \cup \mathcal{T}^{(k)}$ ;
  - 8:   compute  $g^{(k+1)}(\mathbf{p}) := \sum_{i \in \mathcal{I}^{(k+1)}} \alpha_i \varphi_i(\mathbf{p}) + \pi(\mathbf{p})$  such that  $g^{(k+1)}(\mathbf{p}_i) = f(\mathbf{p}_i), i \in \mathcal{I}^{(k+1)}$  (c.f., Eq. (6));
  - 9:   compute  $f^{(k+1)} := g_{\mathcal{P}}^{(k+1)}$ ;
  - 10:   compute the critical points  $\{\mathbf{p}_i, i \in \mathcal{C}^{(k+1)}\}$  of  $f^{(k+1)}$ ;
  - 11:    $k := k + 1$ ;
  - 12: **end while**
- 

and the new ones related to the set  $\mathcal{Q}^{(1)}$ , that is,

$$g^{(2)}(\mathbf{p}_i) = f(\mathbf{p}_i), \quad i \in \mathcal{I}^{(2)} := \mathcal{I}^{(1)} \cup \mathcal{Q}^{(1)} \cup \mathcal{T}^{(1)},$$

where  $\mathcal{T}^{(1)} := \{j \in N(i), i \in \mathcal{Q}^{(1)}\}$  (Figure 3(d)). Analogously to the previous step, we set  $f^{(2)} := g_{\mathcal{P}}^{(2)}$ .

We now describe the general case. Let us suppose that at the iteration  $k$  we have built  $g^{(k)} : \mathbb{R}^3 \rightarrow \mathbb{R}$  such that

$g^{(k)}(\mathbf{p}_i) = f(\mathbf{p}_i), i \in \mathcal{I}^{(k)}$ . Then, we compute the scalar function  $f^{(k)} := g_{\mathcal{P}}^{(k)}$  and evaluate its set  $\{\mathbf{p}_i, i \in \mathcal{C}^{(k)}\}$  of critical points. At step  $(k + 1)$ , the points related to the indices of  $\mathcal{C}^{(k)}$ , and its 1-star vertices, that do not belong to  $\mathcal{I}^{(k)}$  are added as new constraints and we consider the function  $g^{(k+1)}$  such that

$$g^{(k+1)}(\mathbf{p}_i) = f(\mathbf{p}_i), \quad i \in \mathcal{I}^{(k+1)} := \mathcal{I}^{(k)} \cup \mathcal{Q}^{(k)} \cup \mathcal{T}^{(k)},$$

where the set of indices are  $\mathcal{Q}^{(k)} := \{i \in \mathcal{C}^{(k)}, i \notin \mathcal{I}^{(k)}\}$  and  $\mathcal{T}^{(k)} := \{j \in N(i), i \in \mathcal{Q}^{(k)}\}$  (Figure 3(e-j)).

Since at each iteration  $k$  the critical points of  $f^{(k)}$  include those of  $f$ ,  $f^{(k)}$  has  $M + M(k)$  maxima,  $m + m(k)$  minima, and  $s + s(k)$  saddle points. Here,  $m, M, s$  is the number of minima, maxima, saddles of  $(\mathcal{P}, f)$  and  $M(k), m(k), s(k)$  are positive integers. The iteration stops when the critical points of  $f^{(k+1)}$  have been already used to build  $f^{(k)}$ , i.e.  $\mathcal{C}^{(k+1)} \subseteq \mathcal{I}^{(k)}$ . In this case, we have that  $M(k + 1) \equiv m(k + 1) \equiv s(k + 1) \equiv 0$  and therefore  $f^{(k+1)}$  has the same critical points of  $f$ . We conclude that  $g_1 := g^{(k+1)}$  is the solution of the problem stated at the beginning of this section (Figure 3(k-l) and 4). In the worst case, the iterative procedure involves as many steps as the number of vertices divided by the average number of points in the 1-stars of  $\mathcal{P}$ .

Assuming that the scalar function  $f^{(k)}$  is general and Morse, from the Euler formula (1) we get that the additional critical points satisfy the “nullity relation”  $m(k) - s(k) + M(k) = 0$ . The uniqueness of each function  $g^{(k)}$  and its smoothness degree are guaranteed by

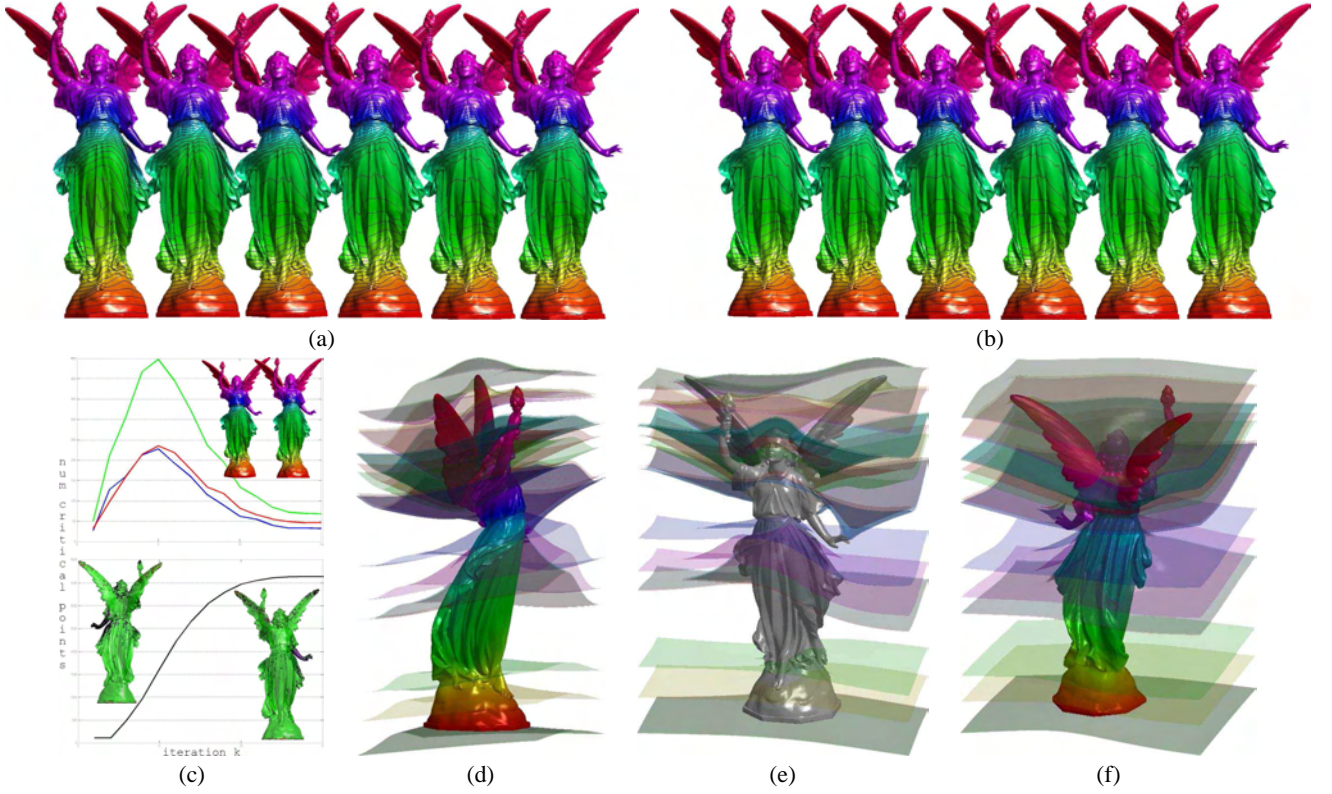


**Figure 6:** (a,b) Level sets of  $f^{(k)}$ ,  $k = 1, \dots, 12$ ; at each iteration  $k$ , the basis functions are centered at the critical points of  $f^{(k)}$  and not at the vertices of their 1-stars. (c) Evolution of the number of critical points and selected centers; the red, blue, and green colors represent the number of maxima, minima, and saddle points. (d-f) Different views on the iso-surfaces of the volume-based approximation of  $f$ .

**Table 1:** With reference to Figure 5, the table shows the number of critical points, 2-saddles, and selected centers.

It.	Max.	Min.	Sad.	2-Sad.	#Cent.	$L^\infty$ -err.
1	20	9	71	0	—	—
2	30	46	118	4	100	0.0957
3	64	38	144	4	1343	0.0783
4	54	17	113	3	2120	0.0751
5	39	11	92	3	2510	0.0690
6	31	12	85	3	2682	0.0691
7	23	9	74	1	2784	0.0683
8	22	9	73	1	2814	0.0682
9	21	10	73	0	2836	0.0683
10	20	9	71	0	2846	0.0683
⋮	⋮	⋮	⋮	⋮	⋮	⋮
14	19	9	70	0	2880	0.0682
15	20	9	71	0	—	0.0683

the theory of the Reproducing Kernel Hilbert Spaces and the regularity of the kernel function [Aronszajn 1950; Poggio and Girosi 1990], respectively. Algorithm 1 summarizes the main steps of the iterative procedure.

### 3.2 Properties of the iterative scheme

Our experiments have shown that if  $f$  has close critical points then a function  $f^{(k)}$  might have saddle points of multiplicity equal to or greater than two (Figure 4, 5, and Table 1). In fact, imposing

that  $f^{(k)}$  interpolates close  $f$ -values at a set  $\mathcal{R}$  of redundant critical points results in a low-varying behavior of  $f^{(k)}$  in a neighborhood of  $\mathcal{R}$  and a higher probability of generating multiple saddles in that region. Our tests have also shown that if  $f$  is general then each approximation  $f^{(k)}$  is general; indeed, the nullity relation is satisfied at each iteration. For more details on the choice of the basis functions, we refer the reader to Section 4. As will be discussed in Section 6, degenerate and redundant critical points with respect to their persistence values can be simplified before running the approximation scheme. In this way, we easily handle noisy scalar functions, which are commonly characterized by very close critical points with low-persistence values.

As shown in Figure 4(b), 5(b), and 6(c), the number of critical points of each approximation  $f^{(k)}$  increases at the beginning of the iterations until a maximum is reached. This behavior is due to the fact that each approximation  $f^{(k)}$  is achieved by using few basis functions, i.e. few interpolating conditions of the  $f$ -values. Then, the number of critical points of  $f^{(k)}$  starts to decrease until it converges to the number of critical points of  $f$ . In fact, at this stage each  $f^{(k)}$  incorporates the global structure of  $f$  and the small discrepancy between  $f^{(k)}$  and  $f^{(k+1)}$ , in terms of number and position of the critical points, forces the insertion of few new centers. Note that the number of selected centers increases with  $k$ .

Even though the computation of  $g_1$  and  $h := g_{1,\mathcal{P}}$  is fully controlled by the distribution of the critical points, the approximation error  $\|f - f^{(k)}\|_\infty$  rapidly decreases to zero with respect to the iteration  $k$ . In fact, a higher number of interpolating conditions is used to compute  $f^{(k)}$  from  $f^{(k-1)}$ ,  $k \geq 1$  (Figure 5(c) and Table 1).



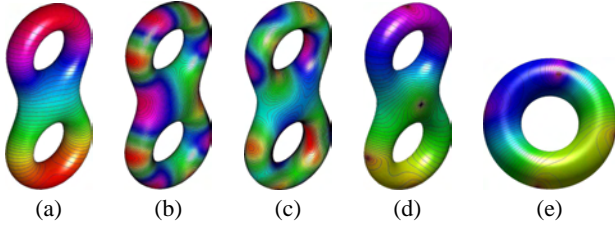


**Figure 7:** Level sets of (a-c) three functions with a different number of critical points, and (d,e) two harmonic maps. The parameters used for their approximation are reported in Table 2 and 3.

**Table 2:** Given the bitorus  $\mathcal{P}$  in Figure 7(a-d) with a different number  $n$  of vertices, we computed four scalar functions  $f_i$ ,  $i = 1, \dots, 4$ , with an increasing number of critical points. The table shows the number  $k_1$  of iterations and  $r_1$  basis functions used to compute the corresponding approximations. The number of centers and iterations slightly vary with respect to the growth of  $n$ .

$f_1 : (M = 1, m = 1, s = 4)$   $f_2 : (M = 11, m = 12, s = 25)$   
 $f_3 : (M = 31, m = 35, s = 68)$   $f_4 : (M = 3, m = 3, s = 6)$

$n$	$f_1$		$f_2$		$f_3$		$f_4$	
	$k_1$	$r_1$	$k_1$	$r_1$	$k_1$	$r_1$	$k_1$	$r_1$
766	4	90	3	169	4	256	3	142
3070	3	134	6	329	4	310	4	196
12286	5	222	6	506	5	469	5	324
49150	5	358	10	967	5	601	8	542

As reported in Figure 7 and Tables 2, 3, the number of iterations and selected centers is slightly affected by a different sampling density of the input surface and/or the choice of a different kernel function. This difference becomes minimal while increasing the number of vertices of  $\mathcal{P}$ . Assuming that the surface  $\mathcal{M}$  underlying the triangle mesh  $\mathcal{P}$  is smooth, the function  $h := g_{\mathcal{P}}$  is a piecewise linear approximation of the restriction  $g|_{\mathcal{M}}$  of  $g$  to  $\mathcal{M}$ .

## 4 Error-driven approximation

This section discusses how the topology-driven scheme can be improved using locally-supported basis functions (Section 4.1). Then, we use the selected centers to define a least-squares approximation without (Section 4.2) or with constraints on the critical points of the input function (Section 4.3). These two variants guarantee the robustness of the approximation against noise. Finally (Section 4.4), we estimate the approximation error.

### 4.1 From topology- to error-driven function approximation

Let us suppose that the approximation  $h := g_{\mathcal{P}}$  of  $f$  has been computed using the topology-driven scheme discussed in Section 3. We now improve the approximation  $h$  of  $f$  by adding to  $g_1$  an error-driven term  $g_2$  such that the error between  $h + g_2$  and  $f$  is below the target approximation accuracy. In this case,  $g_2$  is a linear combination of locally-supported radial basis functions [Wendland 1995] and the center selection is guided by the target accuracy. Therefore,  $f_2$  captures those local details of  $f$  previously neglected.

First of all, we construct the family of nested spaces  $\{\mathcal{V}_k\}_{k=1}^q$  (Section 3.1) such that

$$\mathcal{V}_k := \text{span}\{x, y, z, 1\} \oplus \text{span}\{\varphi_i, i \in \mathcal{I}^{(k)}\},$$

**Table 3:** Given the torus in Figure 7(e) with a different number  $n$  of vertices, the table shows the number  $k_1$  (resp.,  $k_2$ ) of iterations and  $r_1$  (resp.,  $r_2$ ) basis functions used to compute the approximations of the same scalar function using the Gaussian (resp., bi-harmonic) kernel. Fixing the kernel, the number of centers and iterations slightly vary with respect to the growth of  $n$ .

$n$	Kernel function			
	$\varphi(t) := \exp(-t)$		$\varphi(t) :=  t ^3$	
	$k_1$	$r_1$	$k_2$	$r_2$
400	4	110	3	86
1600	4	162	4	267
3600	4	187	5	400
6400	6	242	5	518
10K	5	293	6	640
40K	7	517	7	1148
160K	11	990	7	1546

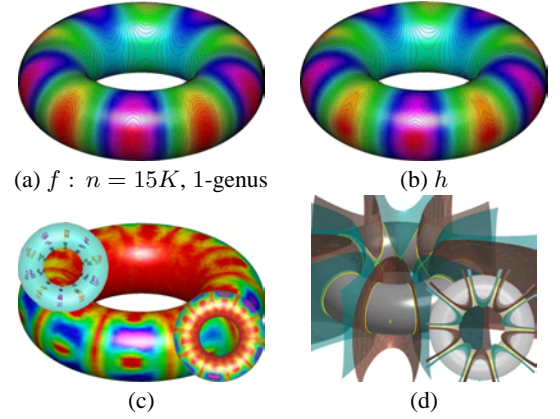


**Figure 8:** (a) Input function  $f$  and (b) its approximation  $h$ . (c)  $L^\infty$ -error between  $f$  and  $h$ , and selected centers. (d) Iso-surfaces of  $g$  at saddles; here, we used the 0.028% and 0.05% of globally- and locally-supported radial basis functions.

$\mathcal{V}_k \subseteq \mathcal{V}_{k+1}$ ,  $g^{(k)} \in \mathcal{V}_k$ . The notation  $\text{span}\{\varphi_i, i \in \mathcal{I}\}$  refers to the linear space generated by the basis functions  $\varphi_i$ ,  $i \in \mathcal{I}$ . Indeed, each approximation  $f^{(k)}$  of  $f$  has a number of critical points greater than  $f$  and is associated to the implicit map  $g^{(k)}$ . At the last iteration  $q$ , we have that the map

$$g_1(\mathbf{p}) := g^{(q)}(\mathbf{p}) := \sum_{i \in \mathcal{I}} \alpha_i \varphi_i(\mathbf{p}) + \beta_0 + \beta_1 x + \beta_2 y + \beta_3 z, \quad (5)$$

$\mathcal{I} := \mathcal{I}^{(q)}$ , is the superposition of  $(r + 4)$  basis functions.

The coefficients  $\alpha := (\alpha_i)_{i \in \mathcal{I}} \in \mathbb{R}^r$ ,  $\beta := (\beta_i)_{i=0}^3 \in \mathbb{R}^4$ , are the solutions of the linear system

$$\tilde{\mathbf{L}}\sigma = \tilde{\mathbf{b}}, \quad \sigma := \begin{bmatrix} \alpha \\ \beta \end{bmatrix} \in \mathbb{R}^{(r+4) \times 1}, \quad (\tilde{\mathbf{L}} := \tilde{\mathbf{L}}^{(q)}), \quad (6)$$

with  $\tilde{\mathbf{b}} := [(f(\mathbf{p}_i))_{i \in \mathcal{I}}, 0, 0, 0, 0]^T \in \mathbb{R}^{(r+4) \times 1}$ .

Assuming that the indices in  $\mathcal{I}$  are  $\{1, \dots, r\}$  and according to (4), the coefficient matrix is

$$\tilde{\mathbf{L}} := \begin{bmatrix} \mathbf{A} & \mathbf{P} & \mathbf{1} \\ \mathbf{P}^T & \mathbf{0} & \mathbf{0} \\ \mathbf{1}^T & \mathbf{0} & \mathbf{0} \end{bmatrix} \in \text{Gl}_{r+4}(\mathbb{R}), \quad \mathbf{A} := (\varphi(\|\mathbf{p}_i - \mathbf{p}_j\|_2))_{i,j \in \mathcal{I}},$$



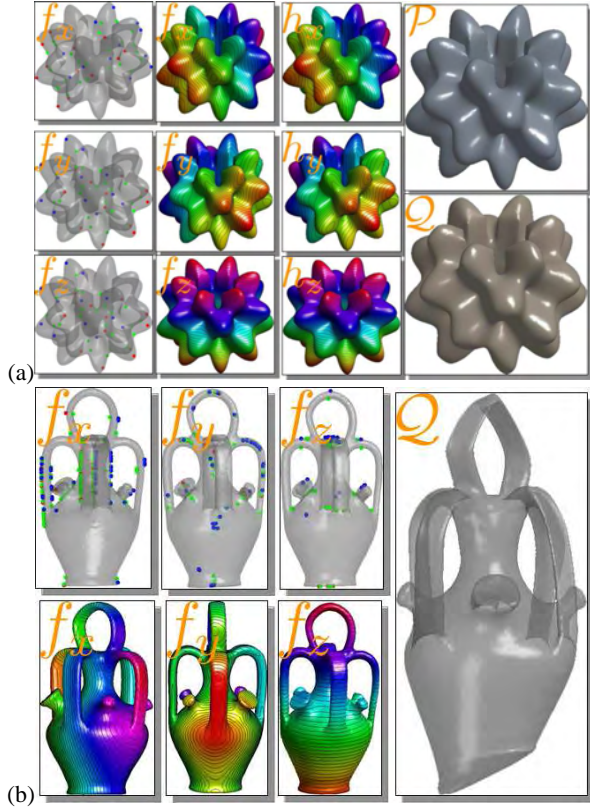


**Figure 9:** (a,b) Given the height functions  $f_x$ ,  $f_y$ , and  $f_z$  on  $\mathcal{P}$  with respect to the coordinates axis, we visualize the corresponding approximations  $h_x$ ,  $h_y$ , and  $h_z$  as a new surface  $\mathcal{Q}$ . Its regularity confirms that the scheme generates smooth approximations. In (b), a larger discrepancy between  $\mathcal{P}$  and  $\mathcal{Q}$  highlights a larger error between the input and the approximated functions.

$\mathbf{P} \in \mathbb{R}^{r \times 3}$  is the matrix whose columns are the  $(x, y, z)$ -coordinates of the points in  $\mathcal{B} := \{\mathbf{p}_i\}_{i \in \mathcal{I}}$ , and  $\mathbf{1} \in \mathbb{R}^{r \times 1}$  is the constant vector whose entries are equal to one. Since the approximation error between  $f$  and  $h$  on the set of points corresponding to  $\mathcal{I}$  is zero, we consider the points of  $\mathcal{P}$  where the error is greater than a given threshold  $\epsilon > 0$ , i.e.  $\mathcal{A} := \{i : |f(\mathbf{p}_i) - h(\mathbf{p}_i)| \geq \epsilon\}$ , and we use  $\mathcal{A}$  to update  $g_1$ . To this end, it is sufficient to compute the new function

$$g(\mathbf{p}) := \underbrace{\sum_{i \in \mathcal{I}} \alpha_i \varphi_i(\mathbf{p})}_{g_1(\mathbf{p}) \text{ glob. supp.}} + \underbrace{\sum_{i \in \mathcal{A}} \alpha_i \phi_i(\mathbf{p})}_{g_2(\mathbf{p}) \text{ loc. supp.}}, \quad \mathbf{p} \in \mathbb{R}^3, \quad (7)$$

that satisfies the interpolating conditions  $g(\mathbf{p}_i) = f(\mathbf{p}_i)$ ,  $i \in \mathcal{I} \cup \mathcal{A}$ . To define  $g_2$ , we also impose that it is zero at the points of  $\mathcal{B} := \{\mathbf{p}_i\}_{i \in \mathcal{I}}$  and at the vertices of the corresponding 1-stars. As error measure to define  $\mathcal{A}$ , we can also use the local distances defined in [Biasotti et al. 2007; Edelsbrunner et al. 2004]. Analogously, the piecewise linear approximations  $g_{1,\mathcal{P}}$  and  $g_{2,\mathcal{P}}$  to  $\mathcal{P}$  provide the *global* and *local component* of  $f$ .

Even though the critical points of  $f$  and  $f_1$  are the same, those of  $h := f_1 + f_2$  and  $f$  might be different; in fact, summing  $f_2$  to  $f_1$  can add or cancel some of the critical points of  $f_1$ . To avoid this case, at each iteration we use the  $f_2$ -values at its critical points and at the vertices of the corresponding 1-stars as interpolating constraints. In our tests, this situation never happened and it is related to special configurations of the critical points.

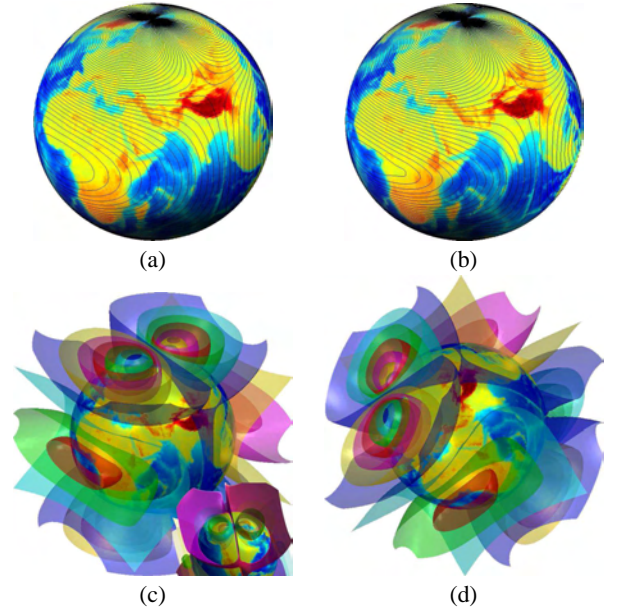


**Figure 10:** (a) Level sets of (a) the magnitude  $f$  of an energy field generated by twelve sources distributed on the earth surface  $\mathcal{P}$  and (b) its approximation  $h := g_{\mathcal{P}}$ . (c,d) Iso-surfaces of  $g$  that represent the behavior of  $f$  around the earth surface. The function  $g$  has been computed with the 2.52% and 31.41% of globally- and locally- supported basis functions ( $\|f - h\|_{\infty} = 0.081$ ).

In (7), the new basis functions  $\{\phi_i\}_{i \in \mathcal{A}}$  are chosen with compact support; in our implementation, we have selected  $\phi(t) := (1 - t)^4(4t + 1) \in C^2([0, 1])$  [Wendland 1995] as sparse kernel (i.e.,  $\phi_i(\mathbf{p}) := \phi(\|\mathbf{p} - \mathbf{p}_i\|_2 / \sigma_i)$ ) and the support  $\sigma_i$  has been set equal to the averaged radius of the 2-star of the vertex  $\mathbf{p}_i$ . Finally, choosing  $\epsilon := 0$  provides the highest approximation accuracy; in fact,  $g$  interpolates all the  $f$ -values, using only a small number of globally-supported radial basis functions (Figure 8).

At each iteration, the evaluation of the critical points of  $f^{(k)}$  takes linear time; in fact, the 1-star structure of  $\mathcal{P}$  is calculated at the first step to initialize the set of centers in (2) and, once stored, it is used at the next steps without any additional overhead. Any approximation  $g^{(k)}$ ,  $k \leq q$ , is a linear combination of  $r_k$  basis functions  $\{\varphi_j\}_{j \in \mathcal{I}^{(k)}}$  and  $\tilde{\mathbf{L}}^{(k)}$  is the corresponding  $(r_k + 4) \times (r_k + 4)$  coefficient matrix in (4). Then, for the construction of  $\tilde{\mathbf{L}}^{(k+1)}$  we calculate only the new elements  $\{\varphi(\|\mathbf{p}_i - \mathbf{p}_j\|_2)\}_{i \in \mathcal{Q}^{(k+1)}, j \in \mathcal{I}^{(k+1)}}$  and insert them in  $\tilde{\mathbf{L}}^{(k)}$ . Modeling the local details of  $f$  with compactly-supported basis functions requires to insert in  $\tilde{\mathbf{L}}$  a sparse sub-matrix, thus guaranteeing the scalability of the proposed approach with respect to the number of vertices of  $\mathcal{P}$  and without creating a bottleneck for the solution of the associated linear system. In Figure 9, we used the approximation scheme to reconstruct the surface geometry of two shapes using the height function with respect to the coordinate axes. The results in Figure 10 and 11 highlight the smoothness of our scheme.

If we assume that  $f$  is computed by sampling an implicit function  $v : \mathbb{R}^3 \rightarrow \mathbb{R}$  on the surface  $\mathcal{P}$ , then we expect that the approximation error between  $v$  and the topology- and/or error-driven approximation  $g$  will be low as long as we are close to the surface. To verify this remark, in Figure 12 the surface  $\mathcal{P}$  has been normalized in such a way that the main diagonal of its bounding box has unitary length and the  $v$ -values belong to the interval  $[0, 1]$ . Until the sam-

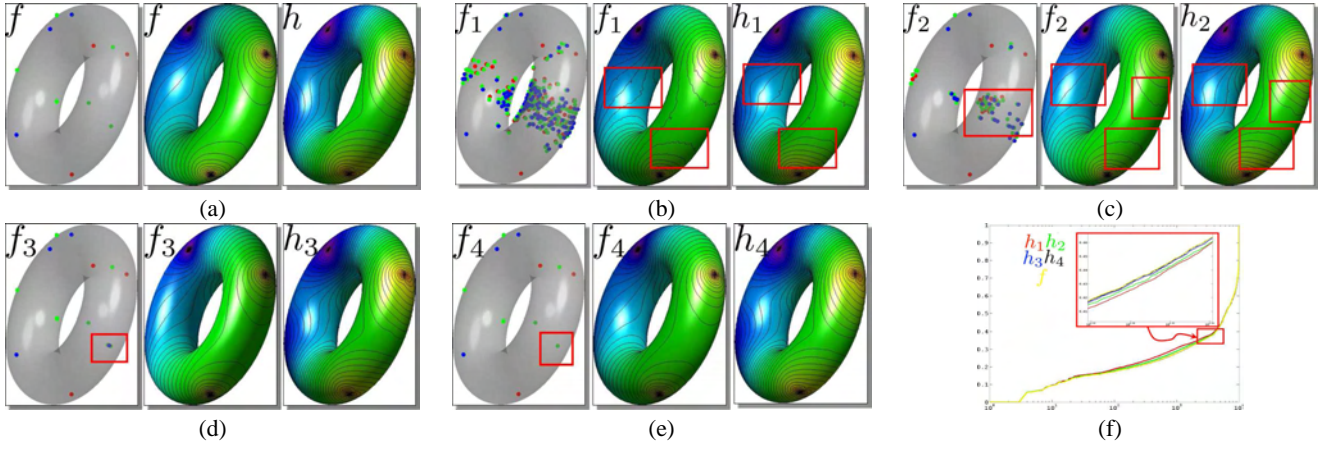


**Figure 11:** Given the function  $f$  in (a), we computed four noisy maps (b-e, left and middle). Each  $f_i$  is achieved by summing to  $f$  a Gaussian noise  $d_{gn}$  with mean zero and standard deviation one, i.e.  $f_i := f + \delta_i d_{gn}$ ,  $i = 1, \dots, 4$  (right). Here,  $\delta_i$  decreases to zero while increasing  $i$ . Each column shows the critical points, the level sets of  $f_i$ , and the approximated function  $h_i$ . The red boxes in (b,c) show that the level sets of  $h_1, h_2$  are smoother than those of  $f_1, f_2$ , thus confirming that the approximation smooths the noise of each  $f_i$ . The red box in (c) shows a set of clustered critical points that disappear in (d). In (f), each  $h_i$  resembles the behavior of  $f$  and  $\|f - h_i\|_\infty \leq 0.01$ ,  $i = 1, \dots, 4$ .

ple points fall inside the unitary sphere centered at the barycenter of  $\mathcal{P}$ , the discrepancy between the corresponding values of  $v$  and  $g$  is lower than 0.1. Moving far from the surface where  $f$  is known increases the approximation error. Maintaining the overall structure of the proposed approach, the accuracy of the approximation of  $v$  around  $\mathcal{P}$  can be improved by using additional interpolating constraints or an *a-priori* information on the underlying phenomenon.

## 4.2 Least-squares function approximation

Once the centers  $\mathcal{B} := \{\mathbf{p}_i := (p_i^x, p_i^y, p_i^z)\}_{i \in \mathcal{I}}$  of the globally-supported basis functions have been identified throughout the topology-driven scheme, we can also compute the best approximation of  $f$  with respect to the least-squares error between  $g_{\mathcal{P}}$  and  $f$ . To this end, we search the function

$$g(\mathbf{p}) := \sum_{i \in \mathcal{I}} \alpha_i \varphi_i(\mathbf{p}) + \beta_0 + \beta_1 x + \beta_2 y + \beta_3 z, \quad \mathbf{p} \in \mathbb{R}^3, \quad (8)$$

that minimizes the least-squares error

$$E(g) := \|g_{\mathcal{P}} - f\|_2^2 := \sum_{i=1}^n |g(\mathbf{p}_i) - f(\mathbf{p}_i)|^2. \quad (9)$$

To compute the unknowns  $(\alpha_i)_{i \in \mathcal{I}} \cup \{\beta_0, \beta_1, \beta_2, \beta_3\}$  in (8), let us introduce the following  $n \times (r+4)$  matrix

$$\mathbf{L} := \begin{bmatrix} a_{11} & a_{12} & \dots & a_{1r} & 1 & p_1^x & p_1^y & p_1^z \\ a_{21} & a_{22} & \dots & a_{2r} & 1 & p_2^x & p_2^y & p_2^z \\ \vdots & \vdots & \vdots & \vdots & \vdots & \vdots & \vdots & \vdots \\ a_{n1} & a_{n2} & \dots & a_{nr} & 1 & p_n^x & p_n^y & p_n^z \end{bmatrix} \quad (10)$$

with coefficients  $\{a_{ij} := \varphi(\|\mathbf{p}_i - \mathbf{p}_j\|_2)\}_{i=1, \dots, n}^{j=1, \dots, r}$  and the vectors

$$\sigma := \begin{bmatrix} \alpha_1 & \dots & \alpha_r & \beta_0 & \beta_1 & \beta_2 & \beta_3 \end{bmatrix}^T \in \mathbb{R}^{(r+4) \times 1},$$

$$\mathbf{b} := \begin{bmatrix} f(\mathbf{p}_1) & \dots & f(\mathbf{p}_n) \end{bmatrix}^T \in \mathbb{R}^{n \times 1}.$$

The functional in (9) can now be rewritten as  $E(g) = \|\mathbf{L}\sigma - \mathbf{b}\|_2^2$  and its minimum is attained at the solution  $\sigma$  of the normal equation  $\mathbf{L}^T \mathbf{L} \sigma = \mathbf{L}^T \mathbf{b}$ ; i.e.,  $\sigma = \mathbf{L}^\dagger \mathbf{b}$ , with  $\mathbf{L}^\dagger := (\mathbf{L}^T \mathbf{L})^{-1} \mathbf{L}^T$  pseudoinverse of  $\mathbf{L}$ . Assuming that  $n$  is large, we do not construct the

$n \times (r+4)$  matrix  $\mathbf{L}$  but we store only the  $(r+4) \times (r+4)$  coefficient matrix  $\mathbf{L}^T \mathbf{L}$  and the right-hand vector  $\mathbf{L}^T \mathbf{b}$ . Then, the solution  $\sigma$  of the corresponding linear system is computed using direct or iterative solvers without explicitly storing the pseudoinverse  $\mathbf{L}^\dagger$ . An example of least-squares approximation of a noisy scalar function is shown in Figure 13.

## 4.3 Function approximation with least-squares constraints on the set of critical points

Let us suppose that  $\mathcal{B} := \{\mathbf{p}_i, i \in \mathcal{I}\}$  is the set of centers which guarantee that the function  $g$  in (8) has the same critical points of  $f$ . In particular, we have that  $g(\mathbf{p}_i) = f(\mathbf{p}_i)$ ,  $i \in \mathcal{I}$ . Using the set of basis functions  $\{\varphi_i(\mathbf{p}) := \varphi(\|\mathbf{p} - \mathbf{p}_i\|_2)\}_{i \in \mathcal{I}}$  centered at the points of  $\mathcal{B}$ , we can attenuate the previous interpolating conditions by imposing that  $g$  approximates all the  $f$ -values but with a greater accuracy on the values of  $f$  at its critical points. This is equivalent to search the function  $g$  that minimizes the functional

$$E(g) := \sum_{i \in \mathcal{I}} |g(\mathbf{p}_i) - f(\mathbf{p}_i)|^2 + \epsilon \sum_{i \in \mathcal{I}^C} |g(\mathbf{p}_i) - f(\mathbf{p}_i)|^2, \quad \epsilon \geq 0, \quad (11)$$

where  $\mathcal{I}^C$  is the complementary of  $\mathcal{I}$  and  $\epsilon$  is a trade-off between the two terms of  $E(g)$ . Note that if  $\epsilon = 0$  then we get the solution to our initial problem (i.e.,  $g_{\mathcal{P}}$  and  $f$  have the same critical points). If  $\epsilon = 1$ , then  $g$  is the least-squares solution of (9). Therefore,  $\epsilon$  is the trade-off between preserving all the critical points of  $f$  and minimizing the least-squares error over all the  $f$ -values. As shown in Figure 13, the constrained least-squares formulation provides a smooth approximation while controlling the final distribution of the critical points.

To compute the minimum of the functional in (11), we observe that  $E(g) = \|\mathbf{L}_1 \sigma - \mathbf{b}_1\|_2^2 + \epsilon \|\mathbf{L}_2 \sigma - \mathbf{b}_2\|_2^2$ , where  $\mathbf{L}_1, \mathbf{L}_2$  are the sub-matrices of  $\mathbf{L}$  in (10) whose rows correspond to the indices in  $\mathcal{I}$  and  $\mathcal{I}^C$ , respectively. Analogously,  $\mathbf{b}_1$  and  $\mathbf{b}_2$  are the sub-vectors of  $\mathbf{b}$  whose entries correspond to the indices in  $\mathcal{I}$  and  $\mathcal{I}^C$ . Indeed, we rewrite  $E(g)$  as

$$E(g) = \left\| \begin{bmatrix} \mathbf{L}_1 \\ \epsilon^{1/2} \mathbf{L}_2 \end{bmatrix} \sigma - \begin{bmatrix} \mathbf{b}_1 \\ \epsilon^{1/2} \mathbf{b}_2 \end{bmatrix} \right\|_2^2,$$

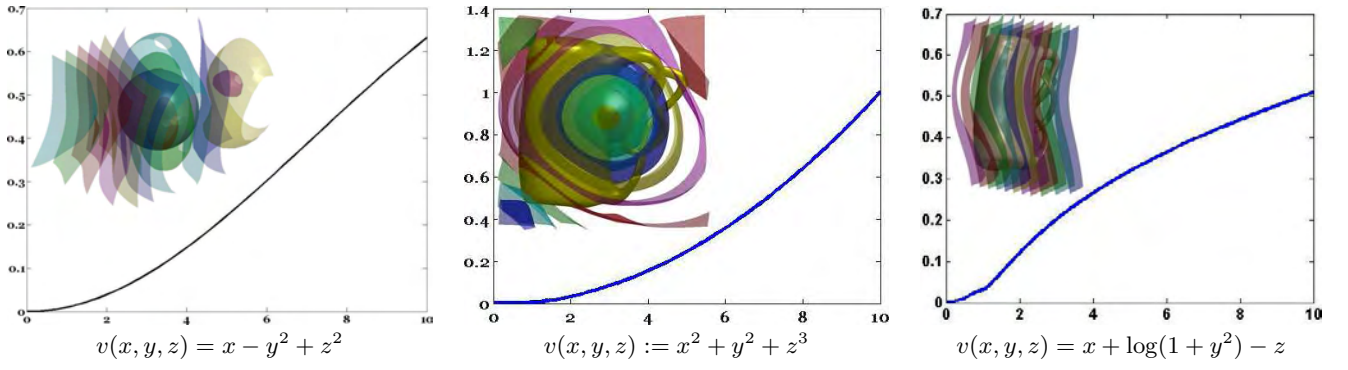


**Figure 12:** Evolution of the  $L^\infty$ -error between a volume-based function  $v(x, y, z)$  and its approximation  $g(x, y, z)$  computed by using the values of  $v$  on a surface  $\mathcal{P}$ . The iso-surfaces are related to  $g$ . The plots show the maximum  $L^\infty$ -error (y-axis) between  $v$  and  $g$  on the points of a set of spheres centered at the barycenter of  $\mathcal{P}$  and with increasing radii (x-axis).

**Table 4:** Computational cost of the main steps of the proposed framework;  $r$  and  $n$  is the number of basis functions and vertices of  $\mathcal{P}$  at the iteration  $k$ . Finally,  $d$  is the number of new basis functions that have been added with respect to the previous iteration.

Task	$k = 1$	$k \geq 2$
Critical point class.	$O(n)$	$O(1)$
Matrix constr./updates	$O(r^2/2)$	$O(nd/2)$
Sol. linear system	$O(r^2)$	$O(r^2)$
Computation of $h$	$O(rn)$	$O(rn)$
Morse Complex simpl.	$O((M + m + s)n)$	–
Least sq./Constrain.	$O(r^2)$	–

whose normal equation  $\nabla E = \mathbf{0}$  is

$$\begin{bmatrix} \mathbf{L}_1^T & \epsilon^{1/2} \mathbf{L}_2^T \end{bmatrix} \begin{bmatrix} \mathbf{L}_1 \\ \epsilon^{1/2} \mathbf{L}_2 \end{bmatrix} \sigma = \begin{bmatrix} \mathbf{L}_1^T & \epsilon^{1/2} \mathbf{L}_2^T \end{bmatrix} \begin{bmatrix} \mathbf{b}_1 \\ \epsilon^{1/2} \mathbf{b}_2 \end{bmatrix};$$

i.e.,

$$\left( \mathbf{L}_1^T \mathbf{L}_1 + \epsilon \mathbf{L}_2^T \mathbf{L}_2 \right) \sigma = \mathbf{L}_1^T \mathbf{b}_1 + \epsilon \mathbf{L}_2^T \mathbf{b}_2. \quad (12)$$

As  $\epsilon$  tends to zero, the interpolating conditions  $g(\mathbf{p}_i) := f(\mathbf{p}_i)$ ,  $i \in \mathcal{I}$ , dominate the value of  $E(g)$  in (11); therefore, the least-squares solution  $g$  is forced to interpolate the values  $\{f(\mathbf{p}_i)\}_{i \in \mathcal{I}}$ . As a consequence, the critical points of  $g_{\mathcal{P}}$  will be the same or close to those of  $f$ . By increasing  $\epsilon$ , we reduce the approximation error  $\|g_{\mathcal{P}} - f\|_2$  and accept a local discrepancy between the critical points of  $g_{\mathcal{P}}$  and  $f$ . The least-squares scheme and smooth basis functions guarantee that this discrepancy is associated to a low number of critical points. We expect that reducing  $\epsilon$  the critical points of  $g_{\mathcal{P}}$  become closer to those of  $f$ . To select the trade-off  $\epsilon$  between smoothness and approximation accuracy, statistical and heuristic methods (e.g.,  $L$ -curve) have been extensively discussed in [Hansen and O’Leary 1993; Wahba 1990]. Figure 13(c) shows the typical  $L$ -curve associated to the functional  $E(g)$  with respect to different choices of  $\epsilon$ . The optimal threshold  $\epsilon$  that minimizes  $E(g)$  gives the best compromise between smoothness and least-squares error. For more details on the  $L$ -curve, we refer the reader to [Hansen and O’Leary 1993].

#### 4.4 Error estimation for the interpolating and least-squares approximation

Let us now consider the error estimation for the interpolating case. Since the  $f$ -values are known on  $\mathcal{P}$ , we estimate the error  $\|g_{\mathcal{P}} - f\|_2$ . Using the notation in Section 4.3 and assuming

that  $g$  is such that  $g_{\mathcal{P}}$  and  $f$  have the same critical points, we have  $g_{\mathcal{P}}(\mathbf{p}_i) = f(\mathbf{p}_i)$ ,  $i \in \mathcal{I}$  and

$$\begin{aligned} E(g) &:= \|g_{\mathcal{P}} - f\|_2^2 = \sum_{i=1}^n |g_{\mathcal{P}}(\mathbf{p}_i) - f(\mathbf{p}_i)|^2 \\ &= \sum_{i \in \mathcal{I}^C} |g_{\mathcal{P}}(\mathbf{p}_i) - f(\mathbf{p}_i)|^2 = \|\mathbf{L}_1 \sigma - \mathbf{b}_1\|_2^2. \end{aligned}$$

From (6),  $\sigma = \tilde{\mathbf{L}}^{-1} \tilde{\mathbf{b}}$  and the error is  $E(g) := \|\mathbf{L}_1 \tilde{\mathbf{L}}^{-1} \tilde{\mathbf{b}} - \mathbf{b}_1\|_2^2$ . Finally, for the least-squares case (12) we have that

$$\begin{aligned} E(g) &= \|\mathbf{L} \sigma - \mathbf{b}\|_2^2 \\ &= \|\mathbf{L}(\mathbf{L}_1^T \mathbf{L}_1 + \epsilon \mathbf{L}_2^T \mathbf{L}_2)^{-1}(\mathbf{L}_1^T \mathbf{b}_1 + \epsilon \mathbf{L}_2^T \mathbf{b}_2) - \mathbf{b}\|_2^2. \end{aligned}$$

Since the remarks in Section 4.2 and 4.3 are independent of the kernel and its support, the previous discussion also applies to the volumetric approximation achieved as superposition of both locally- and globally-supported basis functions (Section 4.1). Table 4 summarizes the computational cost of the proposed framework.

## 5 Properties of the volume- and surface-based approximation

In Section 5.1 and 5.2, we present the main properties of the volumetric function  $g$  and the piecewise linear function  $g_{\mathcal{P}}$ .

### 5.1 Properties of the volume-based approximation $g$

We first discuss the computation of the gradient field and the critical points of the approximation  $g : \mathcal{D} \subseteq \mathbb{R}^3 \rightarrow \mathbb{R}$  of  $f : \mathcal{P} \rightarrow \mathbb{R}$ . Then, we show that the harmonic kernel provides a smooth map  $g$  in the interior of  $\mathcal{P}$ , whose values are a subset of the image of  $f$ .

**Gradient field and upper bound to the energy of  $g$ .** Without loss of generality, we assume that the implicit representation  $g$  is still of the form (5). In fact, we can rewrite (7) as (5) by renaming its terms and separating the indices related to the globally- and compactly-supported basis functions. Indeed, in the following it is not necessary to distinguish between globally- and locally-supported kernels, which are treated in the same manner. Deriving (7), we compute the gradient of  $g$  as

$$\nabla g(\mathbf{p}) = \sum_{i \in \mathcal{I}} \alpha_i \varphi_i'(\mathbf{p}) \frac{\mathbf{p} - \mathbf{p}_i}{\|\mathbf{p} - \mathbf{p}_i\|_2} + (\beta_1, \beta_2, \beta_3), \quad (13)$$



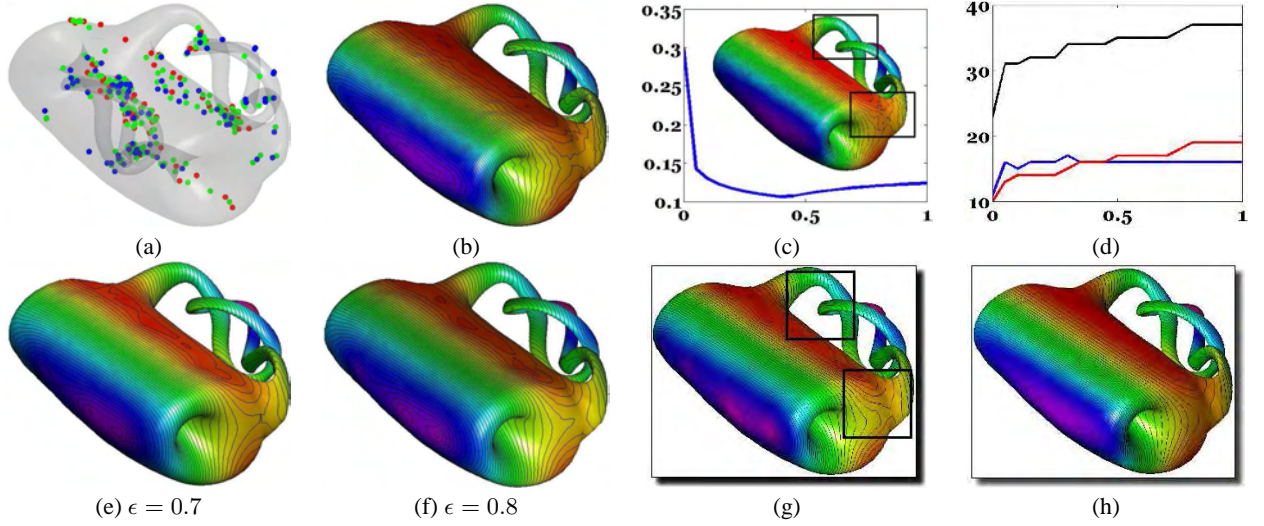


**Figure 13:** (a,b) Critical points and level sets of a noisy function  $f$ . (c) Variation (y-axis) of the least-squares error  $E(g_\epsilon)$  in (11) with respect to several values of the threshold  $\epsilon$  (x-axis). Here,  $g$  has been computed using only the maxima and minima as interpolating constraints. (d) Variation (y-axis) of the critical points of  $h_\epsilon := g_{\epsilon, \mathcal{P}}$  with respect to  $\epsilon$  (x-axis). The red, blue, and black curve shows the number of maxima, minima, and saddles of  $h_\epsilon$ , respectively. (e,f) Level sets of two approximations corresponding to different thresholds. Level sets of (g) the least-squares (9) and (h) constrained least-squares (11) approximation. In (h), we used the threshold  $\epsilon$  which minimizes  $E(g_\epsilon)$ .

where  $\varphi'$  is the derivative of the kernel function  $\varphi$ . From (13), we estimate the energy  $\|\nabla g\|_2$  as follows:

$$\begin{aligned} \|\nabla g(\mathbf{p})\|_2 &\leq \left\| \sum_{i \in \mathcal{I}} \alpha_i \varphi'_i(\mathbf{p}) \frac{\mathbf{p} - \mathbf{p}_i}{\|\mathbf{p} - \mathbf{p}_i\|_2} \right\|_2 + \|\beta\|_2 \\ &\leq \sum_{i \in \mathcal{I}} |\alpha_i| |\varphi'_i(\mathbf{p})| + \|\beta\|_2 \\ &\leq C \|\alpha\|_1 + \|\beta\|_2 \leq C \sqrt{r} \|\alpha\|_2 + \|\beta\|_2, \end{aligned}$$

where  $C := \sup_{t \in \mathbb{R}^+} \{\varphi'(t)\}$ ,  $\alpha := (\alpha_i)_{i \in \mathcal{I}}$ , and  $\beta := (\beta_i)_{i=1}^3$ . Note that  $C$  is finite for most of the kernel functions such as the Gaussian kernel and compactly supported kernels. Using the relation in (6), the previous upper bound becomes

$$\|\nabla g(\mathbf{p})\|_2 \leq \sqrt{r} \lambda_{\max}(\tilde{\mathbf{L}}^{-1}) \|\tilde{\mathbf{b}}\|_2 \leq \sqrt{r} \lambda_{\min}^{-1}(\tilde{\mathbf{L}}) \|\tilde{\mathbf{b}}\|_2.$$

Therefore, the bound to the gradient norm is proportional to the inverse of the minimum eigenvalue of the coefficient matrix  $\tilde{\mathbf{L}}$  and to the norm  $\|\tilde{\mathbf{b}}\|_2$ . In Section 3.1, each basis function has been centered at a point of  $\mathcal{P}$ . However, if we are interested in analyzing the derivatives of  $g$  on  $\mathcal{P}$ , it is sufficient to center the basis functions at the points  $\mathbf{c}_i := \mathbf{p}_i + \delta \mathbf{n}(\mathbf{p}_i)$ ,  $i \in \mathcal{I}$ , close to the vertices of  $\mathcal{P}$  and in the normal direction  $\mathbf{n}(\mathbf{p}_i)$ . Here, the offset value  $\delta$  is proportional to the bounding box of  $\mathcal{P}$  [Morse et al. 2001; Shen et al. 2004; Turk and O'Brien 2002].

**Special choice: volume-based harmonic approximation.** The harmonicity and the minimization of the Dirichlet energy are the most natural ways to characterize the smoothness of an approximation. In this context, the maximum principle of harmonic maps is easily applied to our approach. In fact, the values of  $g$  in the interior of  $\mathcal{P}$  are fully determined by its boundary conditions, which are selected among the  $f$ -values. Using the kernel function  $\varphi(t) := 1/t$  of the 3D Laplacian operator in (3) and during the subsequent iterations, we get that each basis element  $\varphi_i(\mathbf{p})$  is harmonic. Since the function  $\varphi_i(\mathbf{p}) := \|\mathbf{p} - \mathbf{p}_i\|_2^{-1}$  is not defined at  $\mathbf{p}_i$ , the harmonic kernel is centered at the offset points  $\mathbf{c}_i$  previously intro-

duced. In particular,  $g$  is harmonic (i.e.,  $\Delta g = 0$ ) in  $\mathcal{D} := \mathbb{R}^3 \setminus \mathcal{B}$ , with  $\mathcal{B} := \{\mathbf{c}_i\}_{i \in \mathcal{I}}$ , as superposition of harmonic functions.

From the construction of  $g$ , it follows that  $g : \mathcal{D} \rightarrow \mathbb{R}$  is the unique solution of the Laplace equation  $\Delta g(\mathbf{p}) = 0$ ,  $\mathbf{p} \in \mathcal{D}$ , with Dirichlet boundary conditions  $g(\mathbf{p}_i) = f(\mathbf{p}_i)$ ,  $i \in \mathcal{I}$ . Once the boundary constraints have been fixed, the function  $g$  minimizes the Dirichlet energy  $\int_{\mathcal{D}} \|\nabla g(\mathbf{p})\|_2^2 d\mathbf{p}$ . We conclude that the topology-driven approximation  $g$  is a smooth function which minimizes the Dirichlet energy and interpolates the minimal number of  $f$ -values necessary to guarantee that  $f$  and  $g_{\mathcal{P}}$  have the same critical points. In particular, we expect that  $g$  has a low number of critical points.

**Analysis of the critical points of  $g$ .** To compute the critical points of  $g$  we can proceed in two ways. A first approach is to sample the function  $g$  at the nodes of a voxelization  $\mathcal{V}$  of the volume around the input surface  $\mathcal{P}$ . According to [Gerstner and Pajarola 2000], the nodes of  $\mathcal{V}$  are classified as regular or critical on the basis of the number of connected components of the simplified edge graph. In this case, the function values at the nodes are linearly interpolated on each tetrahedron. Alternative approaches are discussed in [Weber et al. 2002; Weber et al. 2007].

A second choice is to classify the nodes of the grid using the values of the gradient field [Hart 1998]. From (13), it follows that  $\mathbf{p} \in \mathbb{R}^3$ ,  $\mathbf{p} \notin \mathcal{B} := \{\mathbf{p}_i\}_{i \in \mathcal{I}}$ , is critical for  $g$  if and only if  $\sum_{i \in \mathcal{I}} \alpha_i \varphi'_i(\mathbf{p}) \frac{\mathbf{p} - \mathbf{p}_i}{\|\mathbf{p} - \mathbf{p}_i\|_2} + (\beta_1, \beta_2, \beta_3) = \mathbf{0}$ . The discrepancy between the smoothness of  $g$  and the discreteness of the voxel grid implies that the values of  $\nabla g$  at the nodes of the grid will not be null. Indeed, we replace the previous condition with an approximate version  $\|\nabla g(\mathbf{p})\|_2 \approx 0$ ; the threshold  $\delta$  used to verify that  $\|\nabla g(\mathbf{p})\|_2 \leq \delta$  is defined on the basis of the values  $\{\|\nabla g(\mathbf{p})\|_2\}_{\mathbf{p} \in \mathcal{V}}$ . As shown in Figure 14, the smoothness of the basis functions guarantees a low number of critical points of  $g$ .

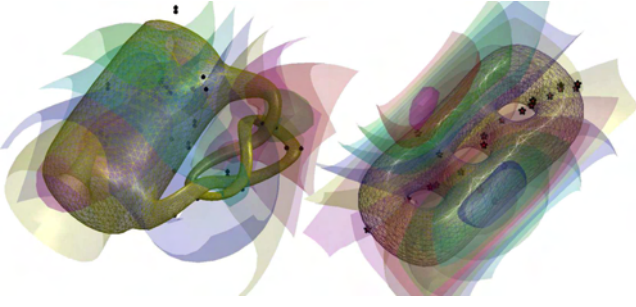


**Figure 14:** The smoothness properties of the approximation guarantees a low number of critical points (black dots).

## 5.2 Properties of the surface-based approximation $g_{\mathcal{P}}$

We now provide a global and a local upper bound to the approximation of  $h := g_{\mathcal{P}}$  to  $f$ , also analyzing the critical points of  $g_{\mathcal{P}}$ .

**Upper bound to the approximation of  $h := g_{\mathcal{P}}$  to  $f$  on  $\mathcal{P}$ .** Without loss of generality, we omit the linear term in (8). While in Section 4.4 we have evaluated the least-squares approximation error  $\|g_{\mathcal{P}} - f\|_2$ , we now derive an upper bound to the error  $\epsilon_k := |g(\mathbf{p}_k) - f(\mathbf{p}_k)|$ ,  $k = 1, \dots, n$ . Since  $g$  interpolates the  $f$ -values  $\{f(\mathbf{p}_k)\}_{k \in \mathcal{I}}$ , we get that  $\epsilon_k = 0$ ,  $k \in \mathcal{I}$ . Let  $j \in \mathcal{I}$  be an index such that  $0 \neq f(\mathbf{p}_j) = \sum_{i \in \mathcal{I}} \alpha_i \varphi_i(\mathbf{p}_j)$  and  $k \notin \mathcal{I}$ . Using the identity  $f(\mathbf{p}_k) = \frac{f(\mathbf{p}_k)}{f(\mathbf{p}_j)} \sum_{i \in \mathcal{I}} \alpha_i \varphi_i(\mathbf{p}_j)$  and the upper bound  $C := \sup_{t \in \mathbb{R}^+} \{|\varphi(t)|\}$  to the kernel  $\varphi$ , from (6) we have that

$$\begin{aligned} |g(\mathbf{p}_k) - f(\mathbf{p}_k)| &= \left| \sum_{i \in \mathcal{I}} \alpha_i \left( \varphi_i(\mathbf{p}_k) - \frac{f(\mathbf{p}_k)}{f(\mathbf{p}_j)} \varphi_i(\mathbf{p}_j) \right) \right| \\ &\leq \sum_{i \in \mathcal{I}} |\alpha_i| \left( |\varphi_i(\mathbf{p}_k)| + \left| \frac{f(\mathbf{p}_k)}{f(\mathbf{p}_j)} \right| |\varphi_i(\mathbf{p}_j)| \right) \\ &\leq C \sum_{i \in \mathcal{I}} |\alpha_i| \left( 1 + \left| \frac{f(\mathbf{p}_k)}{f(\mathbf{p}_j)} \right| \right) \\ &= C \left( 1 + \left| \frac{f(\mathbf{p}_k)}{f(\mathbf{p}_j)} \right| \right) \|\alpha\|_1 \\ &\leq C\sqrt{r} \left( 1 + \left| \frac{f(\mathbf{p}_k)}{f(\mathbf{p}_j)} \right| \right) \|\alpha\|_2 \\ &\leq C\sqrt{r} \left( 1 + \left| \frac{f(\mathbf{p}_k)}{f(\mathbf{p}_j)} \right| \right) |\lambda_{\min}^{-1}(\tilde{\mathbf{L}})| \|\tilde{\mathbf{b}}\|_2 \\ &\leq C\sqrt{r} \left( 1 + \frac{|f(\mathbf{p}_k)|}{\min_{j \in \mathcal{I}^*} \{|f(\mathbf{p}_j)|\}} \right) |\lambda_{\min}^{-1}(\tilde{\mathbf{L}})| \|\tilde{\mathbf{b}}\|_2, \end{aligned}$$

where  $\mathcal{I}^* = \{j \in \mathcal{I}, f(\mathbf{p}_j) \neq 0\}$ . Indeed, the approximation error is bounded by  $\lambda_{\min}^{-1}(\tilde{\mathbf{L}})$  and  $\|\tilde{\mathbf{b}}\|_2$ .

**Upper bound to the approximation of  $h := g_{\mathcal{P}}$  to  $f$  on triangles.** Let us consider the triangle  $\Gamma := (\mathbf{p}_i, \mathbf{p}_j, \mathbf{p}_k)$  of  $\mathcal{P}$  and assume that  $g$  interpolates the  $f$ -values at the vertices of  $\Gamma$ ; therefore, the following relations hold  $f(\mathbf{p}_s) = g(\mathbf{p}_s) = \sum_{l \in \mathcal{I}} \alpha_l \varphi_l(\mathbf{p}_s)$ ,  $s = i, j, k$ . The piecewise linear approximation of  $f$  on the triangle  $\Gamma$  is defined as  $f(\mathbf{p}) := \lambda_1 f(\mathbf{p}_i) + \lambda_2 f(\mathbf{p}_j) + \lambda_3 f(\mathbf{p}_k)$ ,

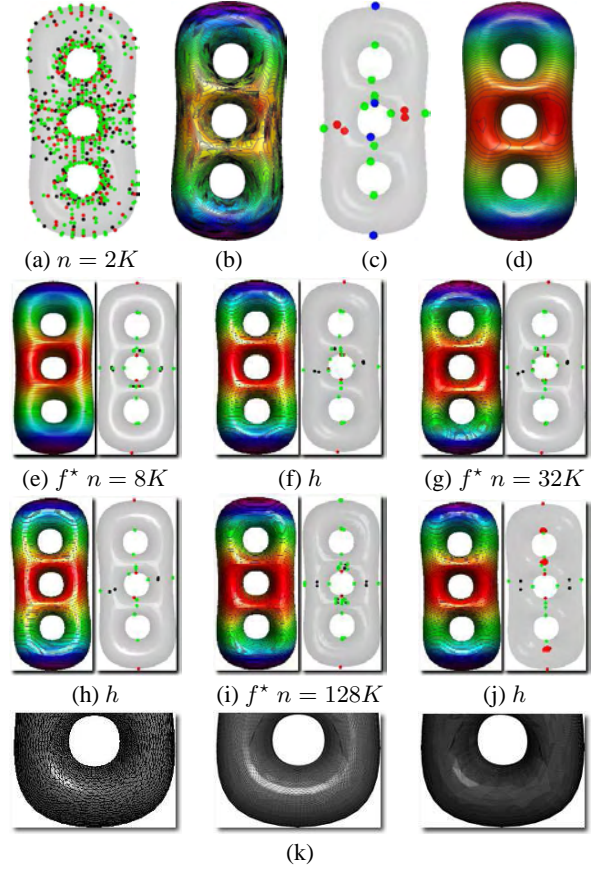


**Figure 15:** (a,c) Critical points and (b,d) level sets of a noisy function  $f$  ( $m = 28$ ,  $M = 32$ ,  $s = 64$ ) and its topology-driven approximation  $h := g_{\mathcal{P}}$  ( $m = 4$ ,  $M = 4$ ,  $s = 12$ ). Level sets and critical points of (e,g,i) the linear interpolation  $f^*$  and (f,h,j) approximation  $h := g_{\mathcal{P}^*}$  on (k) several tessellations  $\mathcal{P}^*$  of  $\mathcal{P}$ .

$\mathbf{p} \in \Gamma$ , with barycentric coordinates  $\lambda_1, \lambda_2, \lambda_3$ . Then,

$$\begin{aligned} |g(\mathbf{p}) - f(\mathbf{p})| &= \left| \lambda_1 \sum_{l \in \mathcal{I}} \alpha_l (\varphi_l(\mathbf{p}) - \varphi_l(\mathbf{p}_i)) + \right. \\ &\quad \left. + \lambda_2 \sum_{l \in \mathcal{I}} \alpha_l (\varphi_l(\mathbf{p}) - \varphi_l(\mathbf{p}_j)) + \lambda_3 \sum_{l \in \mathcal{I}} \alpha_l (\varphi_l(\mathbf{p}) - \varphi_l(\mathbf{p}_k)) \right| \\ &\leq \lambda_1 \sum_{l \in \mathcal{I}} |\alpha_l| |\varphi_l(\mathbf{p}) - \varphi_l(\mathbf{p}_i)| + \lambda_2 \sum_{l \in \mathcal{I}} |\alpha_l| |\varphi_l(\mathbf{p}) - \varphi_l(\mathbf{p}_j)| + \\ &\quad + \lambda_3 \sum_{l \in \mathcal{I}} |\alpha_l| |\varphi_l(\mathbf{p}) - \varphi_l(\mathbf{p}_k)| \leq 2C\sqrt{r} \|\alpha\|_2 \\ &\leq 2C\sqrt{r} \lambda_{\min}^{-1}(\tilde{\mathbf{L}}) \|\tilde{\mathbf{b}}\|_2, \quad C := \sup_{t \in \mathbb{R}^+} \{|\varphi(t)|\}. \end{aligned}$$

Indeed, the upper bound to the approximation error between  $g_{\mathcal{P}}$  and  $f$  on a triangle  $\Gamma$  where  $g$  interpolates the  $f$ -values at the vertices, is proportional to  $\lambda_{\min}^{-1}(\tilde{\mathbf{L}})$  and to  $\|\tilde{\mathbf{b}}\|_2$ .

**Analysis of the critical points of  $g_{\mathcal{P}}$ .** Assuming that we have computed  $g$  as described in Section 3, we evaluate its value at each point of  $\mathcal{P}$  and not only at its vertices. Indeed, we compute the critical points of the piecewise linear function that interpolates the values of  $g$  at the vertices of an over-tessellation  $\mathcal{P}^*$  of the surface  $\mathcal{P}$ . To this end, a new surface  $\mathcal{P}^*$  is generated by subdividing



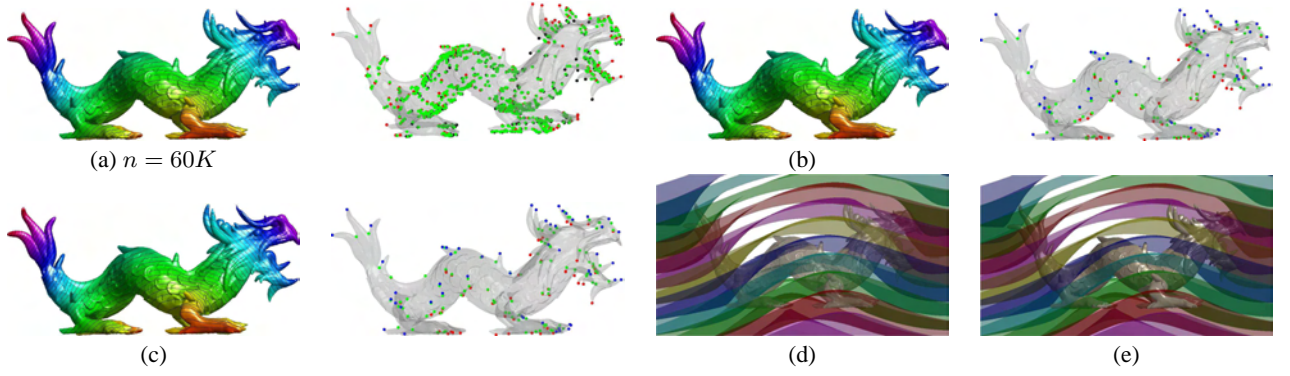


**Figure 16:** (a) Level sets and critical points of a noisy map ( $m = 380$ ,  $M = 390$ ,  $s = 768$ ). Topology-driven approximation achieved using (b, d) all the simplified critical points ( $m = 55$ ,  $M = 61$ ,  $s = 114$ ) and (c, e) only the simplified maxima and minima ( $m = 51$ ,  $M = 55$ ,  $s = 104$ ) as interpolating constraints. In both cases, the shape of the level sets and iso-surfaces are almost the same.

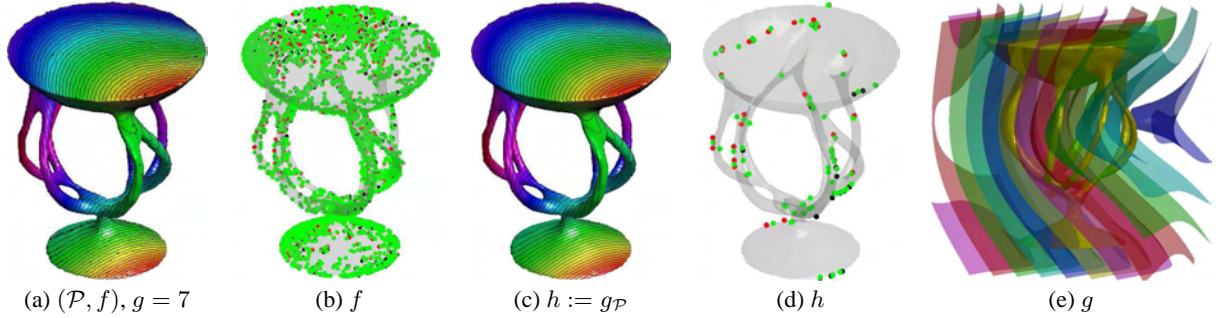


**Figure 17:** Level sets and critical points of (a,b) a noisy map  $f$  with  $m = 1426$  minima,  $M = 1550$  maxima,  $s = 2988$  saddles and (c,d) its smoothed approximation  $h := g_P$  of  $f$ . Here,  $h$  has  $m = 28$  minima,  $M = 25$  maxima, and  $s = 65$  saddles. In  $h$ , the critical points of  $f$  with low-persistence have been smoothed out by the topology-driven approximation and the  $L^\infty$ -error between  $f$  and  $h$  is below 0.001. (e) Iso-surfaces of  $g$ . Note that the level sets in (c) and the iso-surfaces in (e) smoothly resemble the noisy level sets in (a).

each triangle  $t$  of  $\mathcal{P}$  into four sub-triangles by joining the mid-point of each edge of  $t$ . Then, we study the evolution of the critical points of the piecewise linear functions  $g_P$ ,  $g_{P^*}$ , and  $f^*$ . The scalar function  $f^* : \mathcal{P}^* \rightarrow \mathbb{R}$  is computed extending  $f$  from  $\mathcal{P}$  to  $\mathcal{P}^*$  using the linear interpolation of the  $f$ -values; if  $\mathbf{p}$  is a refined vertex of  $\mathcal{P}^*$  and corresponds to the midpoint of the edge  $(i, j)$  of  $\mathcal{P}$ , then we define  $f^*(\mathbf{p}) := (f(\mathbf{p}_i) + f(\mathbf{p}_j))/2$ . By applying several times the previous scheme, we recursively tessellate  $\mathcal{P}^*$  and update the corresponding map  $f^*$ .

Figure 15 shows the evolution of the critical points of the above approximations on the same surface with different tessellations. If  $f$  has a low number of critical points, then the number of critical points of  $f^*$  and  $g_{P^*}$  slightly increases with respect to  $f$ . If  $f$  has a high number of critical points, then the number of critical points of both  $f^*$  and  $g_{P^*}$  remains of the same order and is almost the same. This means that extending  $f$  to the volume around  $\mathcal{P}$  using a smooth function  $g$  resembles the number of critical points of the piecewise linear case. The difference between the number of critical points of  $f^*$ ,  $g_P$  and  $f$  is mainly due to the over-tessellation of the surface  $\mathcal{P}$ . In fact, over-tessellating  $\mathcal{P}$  rapidly increases the number of vertices of  $\mathcal{P}^*$  and the probability of generating discrete critical points when we consider the piecewise linear approximation  $g_{P^*}$ . Comparing (e,f), (g,h), (i,j) in Figure 15, the additional critical points have a low variation of the persistence values; in fact, they belong to the refined 1- or 2-star of a point that is critical at the previous resolution. For each tessellation and for both  $f^*$  and  $h$ , the shape and variation of the level sets is almost the same.

Applying the Loop subdivision to the input surface  $\mathcal{P}$  increases the number of vertices of the subdivided surface  $\mathcal{P}^*$  and improves its smoothness. Our tests have shown that a higher smoothness of  $\mathcal{P}$  produces a lower number of critical points of  $g_{P^*}$  with respect to the over-tessellation. Examples of stability of the approximation scheme with respect to noise are shown in Figure 16 and 17.

## 6 Applications

This section presents three applications of the proposed framework. In Section 6.1, we introduce a simple method for enhancing the visualization of the behavior of  $f$  through the iso-surfaces  $\Sigma_i := \{\mathbf{p} \in \mathbb{R}^3 : g(\mathbf{p}) = f(\mathbf{p}_i)\}$ ,  $i \in \mathcal{C}$ . In Section 6.2, we discuss how a function with a large number of clustered critical points can be approximated by simplifying those that are redundant for the description of  $f$ . Then, Section 6.3 discusses possible variations in the approximation and degenerate cases.

### 6.1 From surface- to volume-based scalar functions: an enhanced visualization approach

The volume-based approximation of  $f$  allows us to approximate  $f$  on the volume  $\mathcal{V}$  around  $\mathcal{P}$ , while preserving key-elements for its description such as the distribution of its critical points and the related function values. To this end, we consider the set  $\{f(\mathbf{p}_i), i \in \mathcal{C}\}$  as representative function values to visualize  $g$  and trace the related iso-surfaces



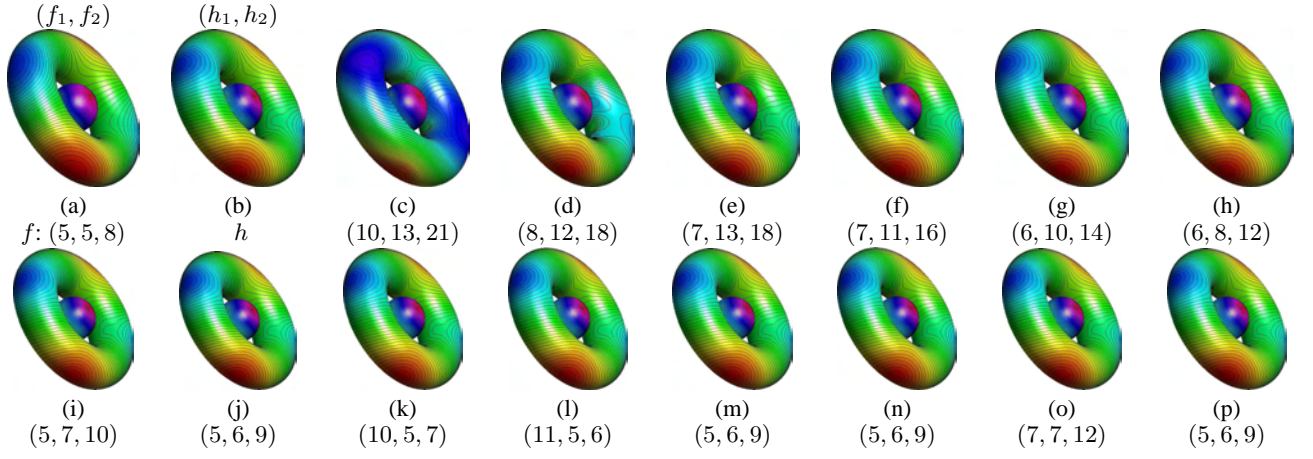


**Figure 18:** (a) Level sets of two maps  $f_1, f_2$  and (b) their approximations  $h_1, h_2$  defined on a torus and a sphere. (c-p) Level sets and critical points  $(M, m, s)$  of the approximations generated by the iterative scheme. The  $L^\infty$ -error between  $(f_1, f_2)$  and  $(h_1, h_2)$  is 0.087.

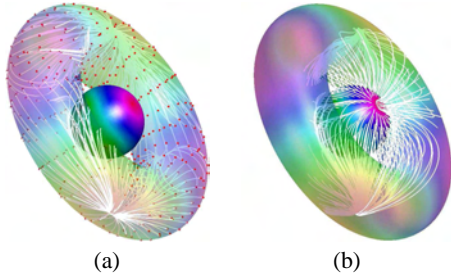


**Figure 19:** Integral lines of  $\nabla g$ , where  $g$  is the volumetric approximation of the maps  $f_1, f_2$  in Figure 18(a): the starting positions of the integral lines are the (a) red and (b) black circles.

$\Sigma_i := \{\mathbf{p} \in \mathbb{R}^3 : g(\mathbf{p}) = f(\mathbf{p}_i)\}, i \in \mathcal{C}$  (Figure 8 and 10). These iso-surfaces and those related to the critical iso-values of  $g$  [Weber et al. 2007] are useful to inspect the behavior of  $g$  on the volume surrounding the input shape and enhance the analysis of  $f$ . As shown in Figure 10(c,d), the smoothness of the iso-surfaces confirms the regularity of  $g$  around and on  $\mathcal{P}$ . Note that the function  $g$  is independent of the resolution of  $\mathcal{P}$  and the voxel grid  $\mathcal{V}$ . Furthermore, its global support allows us to compute the value of the function at each point of the volume around  $\mathcal{P}$  and the approximation accuracy is higher at those points which are closer to  $\mathcal{P}$ . Isosurfacing [Bajaj and Schikore 1998; Stander and Hart 1997; Gerstner and Pajarola 2000; Lorensen and Cline 1987] and volumetric rendering techniques [Fujishiro et al. 2000; Gyulassy et al. 2007; Pascucci et al. 2004; Weber et al. 2007] are used to guarantee that the extracted iso-surfaces have the same topological structure as the original and to enhance the exploration of the properties of  $g$  around  $\mathcal{P}$ .

The proposed approximation strategy can also be used to correlate different phenomena, each represented by a scalar function on the same or on different surfaces. Let us suppose that we know the measurements of a phenomenon on two or more surfaces. These functions might show a common behavior on the regions of different surfaces, changes in their relations, or a similar behavior with respect to a comparison measure [Biasotti et al. 2007; Edelsbrunner et al. 2004]. More precisely, let  $f_i : \mathcal{P}_i \rightarrow \mathbb{R}$  be a scalar function defined on a 2-manifold triangle mesh  $\mathcal{P}_i, i = 1, \dots, l$ . To apply our approximation scheme, we search a smooth function  $g : \mathbb{R}^3 \rightarrow \mathbb{R}$  with global support such that  $g_{\mathcal{P}_i}$  has exactly

the same critical points of  $f_i, i = 1, \dots, l$ . To compute such a function, we proceed as done in Section 3; the only difference is that at the iteration  $(k + 1)$  the approximation  $g^{(k+1)}$  is a linear combination of the radial basis functions centered at each critical point of the scalar functions  $g_{\mathcal{P}_i}^{(k)}, i = 1, \dots, l$ , and at the vertices of the corresponding 1-star (Figure 18(a-p)). Therefore, the critical points of each  $f_i$  contribute to define a *unique* volumetric approximation  $g$ , which is used to compute global descriptors of the interaction among the  $\{f_i\}_{i=1}^l$  such as integral lines, particles, and ribbons of  $\nabla g$  (Figure 19 and 20). Note that  $\nabla g$  is computed by analytically deriving the implicit function (7).

## 6.2 Approximating $f$ with simplified critical points

The topology-driven approximation guarantees that  $g_{\mathcal{P}}$  has the same critical points of  $f$ , which correspond to the nodes of their Morse complexes and are joined by flow lines of steepest ascent/descent (Figure 21). Finally, we expect that the arcs of the complex of  $h$  are smoother than those of  $f$ . Whenever the scalar function  $f$  has a large number of critical points associated to a low variation of the  $f$ -values, it is useful to simplify them and compute a smooth approximation of  $f$  with a lower number of critical points. To this end, [Bremer et al. 2004] defines a topological hierarchy for  $f$  that is constructed by performing a progressive simplification of the Morse complex  $\mathcal{F}$  of  $f$  through the cancellation of pairs of critical points. The importance weight associated to the pair  $(\mathbf{p}_i, \mathbf{p}_j)$  is measured as the *persistence*  $|f(\mathbf{p}_i) - f(\mathbf{p}_j)|$  of  $\mathbf{p}_i, \mathbf{p}_j$ . The local updates of the complex are performed by iteratively removing those pairs with the lowest persistence and reconnecting the neighbors of the removed nodes. Each node removal affects the number and configuration of the critical points of  $\mathcal{F}$  without changing  $f$  or modifying the gradient behavior in the neighborhoods of the cancelled pairs of critical points. Therefore, at the end of the simplification we get a hierarchy for  $f$  where each Morse complex  $\mathcal{F}^{(k)}$  is not associated to a corresponding scalar function  $f^{(k)}$  on  $\mathcal{P}$ . The  $\epsilon$ -simplification [Edelsbrunner et al. 2006] replaces  $f$  with a new function  $h$  such that  $h$  has the same points of persistence of  $f$  higher than a given threshold  $\epsilon$  and the  $L^\infty$ -error between  $f$  and  $h$  is lower than  $\epsilon$ .

In this context, the idea is to build  $h$  by using only the critical points of  $f$  that describe its global behavior and neglecting those that are redundant. To this end, we use the persistence-based simplification to identify the set of critical points which guide the implicit approx-

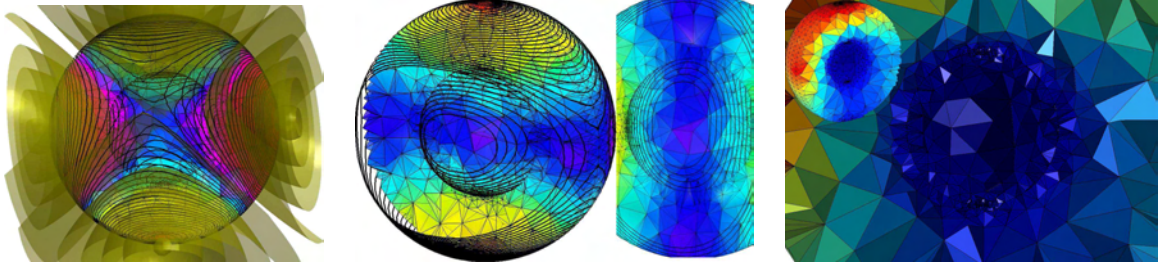


**Figure 20:** Iso-surfaces of the volumetric approximation of two scalar functions defined on two nested spheres.

**Table 5:** Timings (s:ms) related to the main steps of the proposed framework; i.e., the center selection, the construction of the volumetric approximation  $g$  of  $f$ , and the computation of the  $h := g_{\mathcal{P}}$ . Tests are performed on a Pentium IV 2.80 GHz.

Test	#Vert.	#Cent.	#Iter.	Cent. sel.& $g$	$h$
Fig. 1	60K	1011	16	4.18	2.01
Fig. 3, 4	60K	4472	9	4.02	0.80
Fig. 5	280K	2789	16	8.41	2.56
Fig. 6	310K	3613	13	24.58	10.23
Fig. 10	125K	1231	11	6.01	2.46
Fig. 23	65K	975	7	8.01	2.12

imation of  $f$  (Section 3.1). In some cases, it might happen that we get a function  $h$  whose set of critical points *strictly* includes the preserved maxima, minima, and saddles of  $f$ . In fact, let us suppose that the persistence-based simplification discards the critical point  $\mathbf{p} \in \mathcal{P}$  of  $f$  and that it becomes a critical point of  $f^{(k)}$  at the iteration  $k$ . Since  $f^{(k+1)}$  interpolates the  $f$ -values at  $\mathbf{p}$  and at the points of its one star,  $\mathbf{p}$  is a critical point of the final approximation  $h$  of  $f$ . The smoothness of the solution guarantees the reinsertion of a low number of simplified critical points of  $f$  in  $h$ . To avoid this reinsertion, we can proceed as discussed in Section 4.1. Our tests (Figures 1(e-f), 16, 17, 22, 23(d), and 24) have shown that the number and distribution of the critical points of  $h$  still reflect those of  $f$  and the  $L^\infty$ -error between  $f$  and  $h$  is low. The error can be further reduced by adding the error-driven term based on compactly-supported radial basis functions; the number of selected centers at each iteration  $k$  is maintained low by using the  $f$ -values at the extrema of each  $f^{(k)}$  as interpolating conditions.

### 6.3 Scalar functions approximation with weak constraints and treatment of degenerate cases

Since the global structure of  $f$  is reconstructed by a linear combination of globally-supported basis functions, we must ensure that each matrix  $\tilde{\mathbf{L}}^{(k)}$ ,  $k \leq q$ , still fits the available main memory. To address this issue, we devise two main strategies. If  $f$  has a huge number of critical points, which appear clustered into one or more regions, then they are simplified (Section 6.2) before running the approximation scheme. If the critical points have a high persistence, then a strong increase of the simplification rate might delete points that are important to reconstruct the global structure of  $f$ . In this case, we use a low number of globally-supported basis functions by centering locally-supported basis functions at the vertices of the 1-star of each critical point. More precisely, at each iteration we consider as  $\mathcal{T}^{(k+1)} := \mathcal{T}^{(k)} \cup \mathcal{Q}^{(k)}$ , thus neglecting the function values at the vertices of the 1-star of the indices in  $\mathcal{Q}^{(k)}$ , that is, the set  $\mathcal{T}^{(k)} := \{j \in N(i), i \in \mathcal{Q}^{(k)}\}$  (Figure 6).

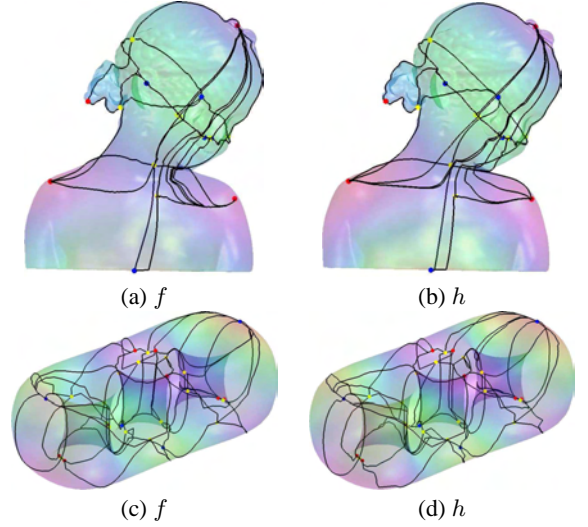


**Figure 21:** Morse complex of (a,c) the input  $f$  and (b,d) the approximate function  $h := g_{\mathcal{P}}$ , where  $g$  is the topology-driven approximation. In both examples, the complexes have a similar structure, include a few number of paths with different shape, and the arcs of the Morse complex of  $h$  are smoother than those of  $f$ .

If  $f$  is not general, then the Euler formula and the nullity relation are not satisfied. A strict inequality in the definition of the maxima, minima, and saddles implies that the points  $\mathcal{R}$  belonging to the edges along which  $f$  is not general are not critical. However, at a given iteration  $k$  the  $f$ -values at  $\mathcal{R}$  become interpolating conditions if a point of  $\mathcal{R}$  belongs to the 1-star of a critical point of  $f^{(k)}$ . We also note that we can force the approximation to interpolate the  $f$ -values along the edges where  $f$  is not general by considering a weak inequality in the definition of the critical points. Even though the Euler formula for  $f^{(k)}$  is not necessarily satisfied, the stop criterion remains unchanged and the stop is usually reached in few iterations (Figure 25 and 26).

To guarantee that  $f$  and its approximation share the same global behavior without having the same critical points, the regularity of the convergence suggests to stop the iterations when the number of critical points in the hierarchy and the centers of the basis functions slightly vary between two consecutive iterations. Regardless the regularity of  $f$  and the sampling density of  $\mathcal{P}$ , the tests presented throughout the paper show that the iterative scheme requires few iterations to converge and the selected centers are a small percentage of the number of input points. Timings are reported in Table 5.



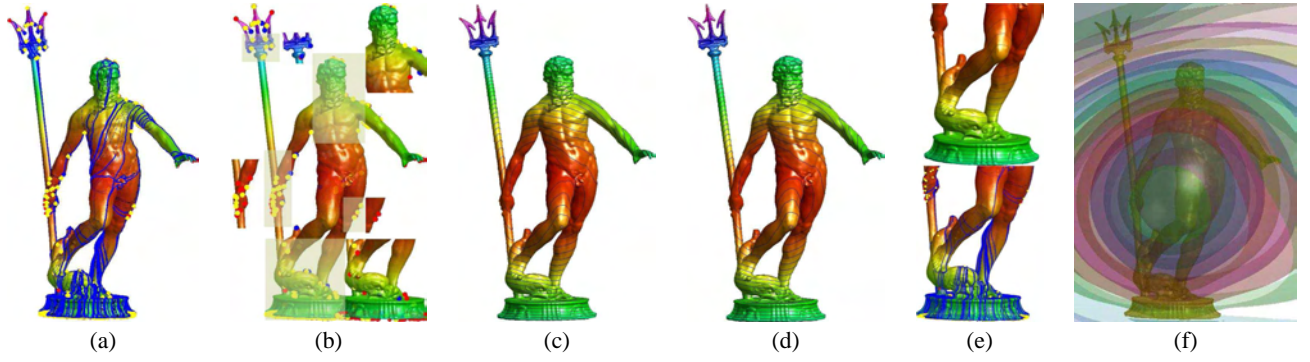


**Figure 22:** (a) Morse complex of a function  $f$  on a 3-genus surface  $\mathcal{P}$ ;  $f$  has  $M = 327$  maxima,  $m = 57$  minima, and  $s = 388$  saddles. (b) The picture shows the critical points that have been maintained in those regions (yellow boxes) where they are clustered. The simplification step has selected 174 maxima, 26 minima, and 204 saddles, i.e. the 57% of the input critical points. (c) Level sets and color map of  $f$  and (d) of the approximated function  $h$ ; the  $L^\infty$ -error between  $f$  and  $h$  is 0.023. (e) Zoom-in on the Morse complex of  $f$  and the level sets of  $h$  in the bottom part of  $\mathcal{P}$ . (f) The iso-surfaces of the volume-based approximation of  $g$  reflect the spherical behavior of  $f$  on  $\mathcal{P}$ .

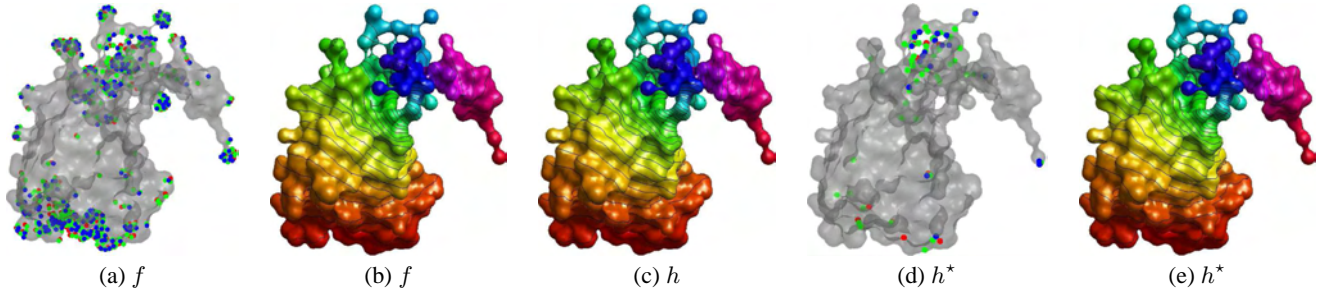


**Figure 23:** (a) Critical points and (b) level sets of an electrostatic charge  $f$  measured on a molecular surface. The function  $f$  has been simulated by placing random charges on the molecular surface. (c) Level sets of the approximated scalar function  $h$  built by maintaining all the critical points of  $f$ ;  $\|f - h\|_\infty = 0.019$ . (d) Simplified set  $\mathcal{S}$  of critical points; few points have been maintained in the bottom part of the molecule due to a low variation of the  $f$ -values on this region. (e) Level sets of the scalar function  $h^*$  built on  $\mathcal{S}$ . Since  $\|f - h^*\|_\infty = 0.023$ , we conclude that the removal of clustered and redundant critical points did not affect the point-wise approximation of  $f$ .

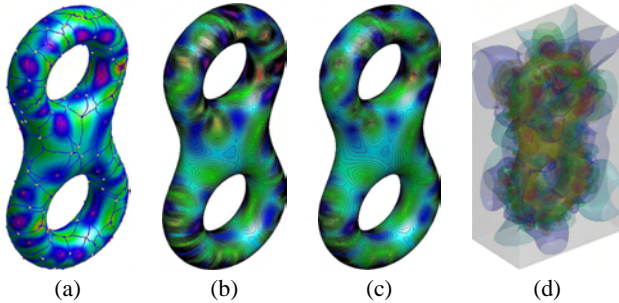


**Figure 24:** (a) Morse complex of a map  $f$  with  $M := 60$  maxima,  $m := 63$  minima, and  $s := 125$  saddles. The simplification has selected the 39% of the critical points of  $f$  (i.e.,  $M := 23$ ,  $m := 24$  minima, and  $s := 49$ ). Level sets of (b)  $f$  and (c) the approximated function  $h$ ;  $\|f - h\|_\infty = 0.081$ . (d) Iso-surfaces of the volumetric approximation of  $f$ .

## 7 Future work

The paper has investigated how the critical points of a given function  $f$  can be used to compute smooth approximations of  $f$  with the same critical points. The proposed topology- and error-driven approximation scheme enables to describe and analyze more func-

tions concurrently defined on several surfaces, as well as their correlation and redundancy. We have demonstrated our method on both synthetic and real data, which include computer graphics, topographic, mechanical, and biomolecular surfaces as well as measurements of the electrostatic charge, mathematical and stress functions. We plan to extend the proposed framework to time-depending and three-dimensional scalar functions. For multi-dimensional functions defined on 2-manifold surfaces, the approximation scheme remains unchanged; in this case, we treat each component of  $f$  separately. Then, the visualization can be addressed by fixing a number of variables and drawing the iso-surfaces with respect to the remaining free parameters, applying a multi-dimensional scaling, or using state-of-the-art techniques developed for the visualization of multi-dimensional data.

## Acknowledgments

This work has been partially supported by FOCUS K3D Coordination Action and the Italy-Israel bilateral project SHALOM. We acknowledge the precious comments of the anonymous reviewers and Prof. Abel Gomes (University of Beira Interior – Portugal), which helped us to improve the content of our work. Models are courtesy of the AIM@SHAPE and the Stanford 3D Scanning Repository, Carlo Sequin (University of Berkely), Tao Ju and Cindy Grimm (Washington University in St. Louis).



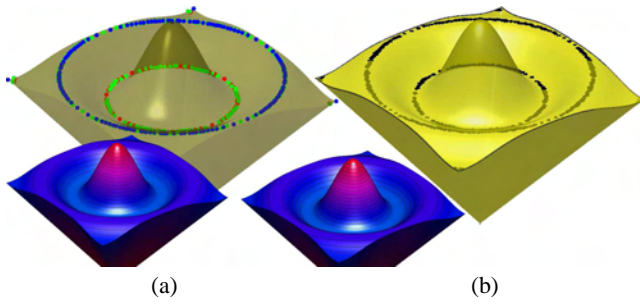


**Figure 25:** (a) Height function  $f$  with respect to the  $z$ -axis on a vulcano rim and (b) its smooth approximation  $h$ . Both  $f$  and  $h$  are not general; the evolution of the critical points is:  $f^{(1)}$ :  $M = 154$ ,  $m = 91$ ,  $s = 232$ ,  $r = 2720$ ;  $f^{(2)}$ :  $M = 155$ ,  $m = 91$ ,  $s = 237$ ,  $r = 2754$ ;  $f^{(3)}$ :  $M = 155$ ,  $m = 91$ ,  $s = 244$ ,  $r = 2768$ . From the fourth step on, the critical points of the current approximation remains unchanged and the iterative procedure stops.

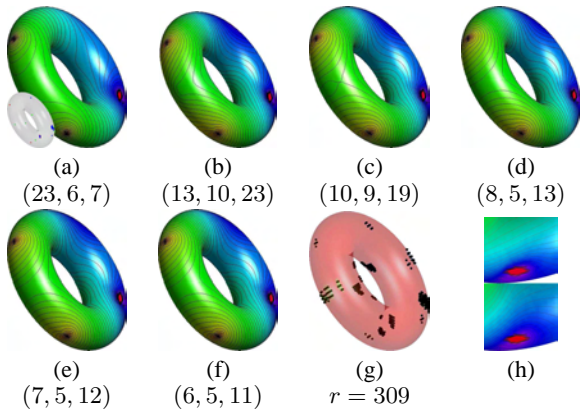


**Figure 26:** (a) Scalar function  $f$  with five 1-stars where  $f$  is not general: one is visible in the bottom-left part of the torus (see also the red region in (h)). (b-f) Approximating functions  $f^{(k)}$ ,  $k = 1, \dots, 5$  and critical points  $(M, m, s)$ ; (g) selected centers; (h) zoom-in on the region where  $f$  and  $h := f^{(5)}$  are not general.

## References

- ARONSZAJN, N. 1950. Theory of reproducing kernels. *Transactions of the American Mathematical Society* 68, 337–404.
- BAJAJ, C. L., AND SCHIKORE, D. R. 1998. Topology preserving data simplification with error bounds. *Computers and Graphics* 22, 1, 3–12.
- BANCHOFF, T. 1967. Critical points and curvature for embedded polyhedra. *Journal of Differential Geometry* 1, 245–256.
- BELKIN, M., AND NIYOGI, P. 2003. Laplacian eigenmaps for dimensionality reduction and data representation. *Neural Computation* 15, 6, 1373–1396.
- BIASOTTI, S., FALCIDIENO, B., DE FLORIANI, L., FROSINI, P., GIORGI, D., LANDI, C., PAPALEO, L., AND SPAGNUOLO, M. Describing shapes by geometric-topological properties of real functions. *ACM Computing Surveys* 40, 4.
- BIASOTTI, S., PATANÈ, G., SPAGNUOLO, M., AND FALCIDIENO, B. 2007. Analysis and comparison of real functions on triangulated surfaces. *Modern Methods in Mathematics*, 41–50.
- BLOOMENTHAL, J., AND WYVILL, B., Eds. 1997. *Introduction to Implicit Surfaces*. Morgan Kaufmann Publishers Inc.
- BREMER, P.-T., EDELSBRUNNER, H., HAMANN, B., AND PASCUCCI, V. 2004. A topological hierarchy for functions on triangulated surfaces. *IEEE Transactions on Visualization and Computer Graphics* 10, 4, 385–396.
- CARR, J. C., BEATSON, R. K., CHERRIE, J. B., MITCHELL, T. J., FRIGHT, W. R., MCCALLUM, B. C., AND EVANS, T. R. 2001. Reconstruction and representation of 3D objects with radial basis functions. In *ACM Siggraph*, 67–76.
- CHEN, S., AND WIGGER, J. 1995. Fast orthogonal least squares algorithm for efficient subset model selection. *IEEE Transactions on Signal Processing* 43, 7, 1713–1715.
- CIPRIANO, G., AND GLEICHER, M. 2007. Molecular surface abstraction. *IEEE Transactions on Visualization and Computer Graphics* 13, 6, 1608–1615.
- CO, C. S., HECKEL, B., HAGEN, H., HAMANN, B., AND JOY, K. 2003. Hierarchical clustering for unstructured volumetric scalar fields. In *IEEE Visualization*, 43.
- CORTES, C., AND VAPNIK, V. 1995. Support-vector networks. *Machine Learning* 20, 3, 273–297.
- DEY, T. K., AND SUN, J. 2005. An adaptive MLS surface for reconstruction with guarantees. In *ACM Symposium on Geometry Processing*, 43–52.
- DONG, S., BREMER, P.-T., GARLAND, M., PASCUCCI, V., AND HART, J. C. 2006. Spectral surface quadrangulation. In *ACM Siggraph*, 1057–1066.
- DYN, N., LEVIN, D., AND RIPPA, S. 1986. Numerical procedures for surface fitting of scattered data by radial functions. *SIAM Journal on Scientific and Statistical Computation* 7(2), 639–659.
- EDELSBRUNNER, H., HARER, J., NATARAJAN, V., AND PASCUCCI, V. 2004. Local and global comparison of continuous functions. In *IEEE Visualization*, 275–280.
- EDELSBRUNNER, H., MOROZOV, D., AND PASCUCCI, V. 2006. Persistence-sensitive simplification functions on 2-manifolds. In *Proc. of the Symposium on Computational Geometry*, ACM, 127–134.
- FUJISHIRO, I., TAKESHIMA, Y., AZUMA, T., AND TAKAHASHI, S. 2000. Volume data mining using 3d field topology analysis. *IEEE Computer Graphics Applications* 20, 5, 46–51.
- GERSTNER, T., AND PAJAROLA, R. 2000. Topology preserving and controlled topology simplifying multiresolution isosurface extraction. In *IEEE Visualization*, 259–266.
- GIROSI, F. 1998. An equivalence between sparse approximation and support vector machines. *Neural Computation* 10, 6, 1455–1480.
- GYULASSY, A., NATARAJAN, V., PASCUCCI, V., AND HAMANN, B. 2007. Efficient computation of Morse-Smale complexes for three-dimensional scalar functions. *IEEE Transactions on Visualization and Computer Graphics* 13, 6, 1440–1447.
- HANSEN, P. C., AND O’LEARY, D. P. 1993. The use of the  $l$ -curve in the regularization of discrete ill-posed problems. *SIAM Journal of Scientific Computing* 14, 6, 1487–1503.
- HART, J. C. 1998. Morse theory for implicit surface modeling. In *Mathematical Visualization*. Springer-Verlag, 257–268.

- HONG, W., NEOPYTOU, N., AND KAUFMAN, A. 2006. Constructing 3D elliptical gaussian for irregular data. In *Mathematical Foundations of Scientific Visualization, Computer Graphics, and Massive Data Visualization*.
- JANG, Y., WEILER, M., HOPF, M., HUANG, J., EBERT, D. S., GAITHER, K. P., AND ERTL, T. 2004. Interactively visualizing procedurally encoded scalar fields. In *VisSym*, 35–44, 339.
- JANG, Y., BOTCHEN, R. P., LAUSER, A., EBERT, D. S., GAITHER, K. P., AND ERTL, T. 2006. Enhancing the interactive visualization of procedurally encoded multifield data with ellipsoidal basis functions. *Computer Graphics Forum* 25, 3, 587–596.
- JOLLIFFE, I. T. 1986. Principal component analysis. In *Principal Component Analysis*. Springer Verlag.
- KANAI, T., OHTAKE, Y., AND KASE, K. 2006. Hierarchical error-driven approximation of implicit surfaces from polygonal meshes. In *Proc. of Symposium on Geometry Processing*, 21–30.
- LI, X., GUO, X., WANG, H., HE, Y., GU, X., AND QIN, H. 2007. Harmonic volumetric mapping for solid modeling applications. In *Proc. of Symposium on Solid and Physical Modeling*, 109–120.
- LIU, Y.-S., LIU, M., KIHARA, D., AND RAMANI, K. 2007. Salient critical points for meshes. In *Proc. of Symposium on Solid and Physical Modeling*, 277–282.
- LLOYD, S. 1982. An algorithm for vector quantizer design. *IEEE Transaction on Communications* 28, 7, 84–95.
- LORENSEN, W. E., AND CLINE, H. E. 1987. Marching cubes: A high resolution 3D surface construction algorithm. *ACM Siggraph* 21, 4, 163–169.
- MADSEN, K., NIELSEN, H. B., AND TINGLEFF, O., 2004. Methods for non-linear least squares problems (2nd ed.).
- MARTIN, T., COHEN, E., AND KIRBY, M. 2008. Volumetric parameterization and trivariate B-spline fitting using harmonic functions. In *Proc. of Symposium on Solid and Physical Modeling*, 269–280.
- MICCHELLI, C. A. 1986. Interpolation of scattered data: Distance matrices and conditionally positive definite functions. *Constructive Approximation* 2, 11–22.
- MILNOR, J. 1963. *Morse Theory*, vol. 51 of *Annals of Mathematics Studies*. Princeton University Press.
- MITRA, N. J., AND NGUYEN, A. 2003. Estimating surface normals in noisy point cloud data. In *Proc. of Symposium on Computational Geometry*, 322–328.
- MORSE, B. S., YOO, T. S., CHEN, D. T., RHEINGANS, P., AND SUBRAMANIAN, K. R. 2001. Interpolating implicit surfaces from scattered surface data using compactly supported radial basis functions. In *Proc. of Shape Modeling International*, 89–98.
- NI, X., GARLAND, M., AND HART, J. C. 2004. Fair Morse functions for extracting the topological structure of a surface mesh. In *ACM Siggraph*, 613–622.
- OHTAKE, Y., BELYAEV, A., ALEXA, M., TURK, G., AND SEIDEL, H.-P. 2003. Multi-level partition of unity implicit surfaces. *ACM Siggraph* 22, 3, 463–470.
- OHTAKE, Y., BELYAEV, A., AND SEIDEL, H.-P. 2005. 3D scattered data interpolation and approximation with multilevel compactly supported RBFs. *Graphical Models* 67, 3, 150–165.
- OHTAKE, Y., BELYAEV, A. G., AND ALEXA, M. 2005. Sparse low-degree implicit surfaces with applications to high quality rendering, feature extraction, and smoothing. In *Proc. of Symposium on Geometry Processing*, 149–158.
- PASCUCCI, V., COLE-MCLAUGHLIN, K., AND SCORZELLI, G. 2004. Multi-resolution computation and presentation of contour trees. In *IASTED conference on Visualization, Imaging, and Image Processing*, 452–290.
- PATANÈ, G., AND FALCIDIENO, B. 2009. Computing smooth approximations of scalar functions with constraints. *Computer & Graphics* 33, 3, 399 – 413.
- PATANÈ, G. 2006. SIMS: a multi-level approach to surface reconstruction with sparse implicit surfaces. In *Proc. of Shape Modeling and Applications*, 222–233.
- POGGIO, T., AND GIROSI, F. 1990. Networks for approximation and learning. *Proceedings of the IEEE* 78, 9, 1481–1497.
- SCHOELKOPF, B., AND SMOLA, A. J. 2002. *Learning with Kernels*. The MIT Press.
- SHEN, C., O'BRIEN, J. F., AND SHEWCHUK, J. R. 2004. Interpolating and approximating implicit surfaces from polygon soup. *ACM Transactions on Graphics* 23, 3, 896–904.
- STANDER, B. T., AND HART, J. C. 1997. Guaranteeing the topology of an implicit surface polygonization for interactive modeling. In *ACM Siggraph*, 279–286.
- STEINKE, F., SCHÖLKOPF, B., AND BLANZ, V. 2005. Support vector machines for 3D shape processing. *Computer Graphics Forum* 24, 3, 285–294.
- TAUBIN, G. 1995. A signal processing approach to fair surface design. In *ACM Siggraph*, 351–358.
- TURK, G., AND O'BRIEN, J. F. 2002. Modelling with implicit surfaces that interpolate. *ACM Transactions on Graphics* 21, 4, 855–873.
- WAHBA, G. 1990. *Spline Models for Observational Data*, vol. 59 of *CBMS-NSF Regional Conference Series in Applied Mathematics*. SIAM, Philadelphia.
- WALDER, C., SCHÖLKOPF, B., AND CHAPPELLE, O. 2006. Implicit surface modelling with a globally regularised basis of compact support. *Computer Graphics Forum* 25, 3, 635–644.
- WEBER, G. H., SCHEUERMANN, G., HAGEN, H., AND HAMANN, B. 2002. Exploring scalar fields using critical iso-values. In *IEEE Visualization*, 171–178.
- WEBER, G., BREMER, P.-T., AND PASCUCCI, V. 2007. Topological landscapes: A terrain metaphor for scientific data. *IEEE Transactions on Visualization and Computer Graphics* 13, 6, 1416–1423.
- WEILER, M., BOTCHEN, R., STEGMAIER, S., ERTL, T., HUANG, J., JANG, Y., EBERT, D. S., AND GAITHER, K. P. 2005. Hardware-assisted feature analysis and visualization of procedurally encoded multifield volumetric data. *IEEE Computer Graphics Applications* 25, 5, 72–81.
- WENDLAND, H. 1995. Real piecewise polynomial, positive definite and compactly supported radial functions of minimal degree. *Advances in Computational Mathematics* 4(4), 389–396.
- XIE, H., McDONNELL, K. T., AND QIN, H. 2004. Surface reconstruction of noisy and defective data sets. In *IEEE Visualization*, 259–266.